Analytical initial conditions and an analysis of baroclinic instability waves in f- and β-plane 3D channel models

P. A. Ullrich[a*], K. A. Reed[b] and C. Jablonowski[c]

[a] *Department of Land, Air and Water Resources, University of California, Davis, CA, USA*
[b] *School of Marine and Atmospheric Sciences, Stony Brook University, Stony Brook, New York, USA*
[c] *Department of Atmospheric, Oceanic & Space Sciences, University of Michigan, Ann Arbor, MI, USA*

*Correspondence to: P. A. Ullrich, Department of Land, Air and Water Resources, University of California, Davis, One Shields Ave., Davis, CA 95616. Email: paullrich@ucdavis.edu

The paper presents a description of idealized, balanced initial conditions for dry 3D channel models with either the hydrostatic or non-hydrostatic shallow-atmosphere equation set. Both the analytical expressions for an f- and β-plane configuration are provided and possible variations are discussed. The initialization with an overlaid perturbation is then used for baroclinic instability studies which can either serve as a test case for the numerical discretization or for physical science investigations such as the impact of the Coriolis parameter on the evolution of baroclinic waves.
Example results for two channel models are presented which are MCore and the Weather Research and Forecasting (WRF) model. The simulations show that the evolution of the baroclinic wave on the β-plane is more unstable than the corresponding f-plane configuration, experiencing a faster linear growth rate of the most unstable wave mode, a shorter most unstable wavelength, a narrower meridional width, and an earlier breaking of the baroclinic wave. A theoretical analysis based on linearized quasi-geostrophic (QG) theory sheds light on these findings. It is shown that the simulated baroclinic instability waves on both the f- and β-plane closely match the predicted wavelength, shape and linear growth rate obtained from the QG theory which validates the model results.

Key Words: Baroclinic instability; dynamical core; test case; non-hydrostatic channel models; f- and β-plane; Coriolis parameter; linear quasi-geostrophic theory

Received . . .

1. Introduction

Baroclinic waves are of fundamental importance in the Earth's atmosphere. They represent the synoptic-scale patterns of high and low pressure systems in the midlatitudes, and are the main exchange mechanism for energy and momentum between the tropical and polar regions. Baroclinic waves and baroclinic instabilty have therefore been of interest to the modeling community for decades, as e.g. documented by Schär and Wernli (1993) and previous authors listed therein. In particular, idealized simulations of different baroclinic wave life cycles, such as the cyclonic versus anticyclonic life cycle with the very different behavior of the upper-air trough, have helped shed light on their dependence on the initial background conditions. Such life cycle aspects have, for example, been discussed by Simmons and Hoskins (1978) and Thorncroft *et al.* (1993) who used global spectral transform models in spherical geometry.

Besides global models, 3D channel models with either the f- or β-plane approximation of the Coriolis parameter are also popular tools to investigate the fundamental behavior of baroclinically unstable flows. Channel models are often less expensive to run from a computational viewpoint, and provide good representation of the midlatitudinal flow which is mostly governed by synoptic-scale sequences of high and low pressure systems. These are often closely approximated by quasi-geostropic theory. Therefore, a wide variety of equation sets have been used for channel models, ranging from the semi-geostrophic equations, primitive equations to the non-hydrostatic Euler equations with the shallow-atmosphere approximation. An issue, that arises for all these equation sets, is the choice of the initial conditions for baroclinic wave experiments. A typical initial state consists of a hydrostatically and geostrophically balanced atmosphere in thermal wind balance that is overlaid with a perturbation. This perturbation acts as a trigger for the evolution of the baroclinic wave.

Defining such a balanced initial base state is not necessarily straightforward since it needs to be a steady-state solution to the equation set. In addition, it needs to provide certain physical characteristics such as static stability and a zonal jet with strong vertical wind shear which makes the atmosphere baroclinically unstable. Furthermore, the initial state should be easy to generate, easy to modify and should allow exact reproducibility by other

modelers. These criteria are at the very core of this paper. They provide motivation for the definition of balanced initial conditions for hydrostatic and non-hydrostatic channel models, that are built upon analytical expressions. These can be evaluated on any model grid and are versatile since they e.g. provide a switch between the f- and β-plane configurations for channel models. The initial conditions presented in this paper can also be easily modified if other physical characteristics are desired, such as a meridional (barotropic) shear of the background zonal wind or the inclusion of moisture. This is important since the evolution of baroclinic instability waves depends on the background conditions as mentioned above, and a technique for the generation of flexible initial states opens up wide application areas.

Unfortunately, almost none of the initial states used in the published literature for baroclinic wave studies fulfill these criteria. A notable exception is the in-depth description of the balanced f-plane background state by Wang and Polvani (2011) that nevertheless still relies on numerical integrations and an iterative procedure for the overlaid perturbation. More recently, Terpstra and Spengler (2015) proposed a methodology that removes the need for iteration but still relies on numerical integration for constructing the basic state. The by-far dominant technique for channel models uses an $f-$plane configuration and prescribes a zonally-invariant, constant, small potential vorticity (PV) value in the troposphere (like 0.4 PV units (PVU)) and a large PV value (like 4 PVU) in the stratosphere. In addition, a dividing line, such as a hyperbolic tangent profile in the meridional direction, is defined between the two regimes, before the 2D PV distribution is numerically inverted via an iterative technique and chosen boundary conditions. However, the resulting initial data set is typically not fully balanced. Therefore, it is further smoothed in an iterative fashion. This technique is for example outlined in Zhang (2004), Plougonven and Snyder (2007) or Waite and Snyder (2009), and was inspired by the method in Rotunno (1994). Davis (2010) extended this PV inversion technique to allow for β-plane variations of the initial data set in a moist environment. However, none of the groups disclosed the full details of their initializations so that their experiments cannot be easily reproduced. Furthermore, there is no agreement on the form of the overlaid perturbation. Some groups like Plougonven and Snyder (2007) or Waite and Snyder (2009) prefer an iteratively computed, unbalanced normal mode perturbation of the most unstable wave. Others like Zhang (2004) define a localized, balanced PV perturbation before the PV inversion is initiated.

The purpose of this paper is twofold. First, we provide a thorough description of idealized, balanced, analytical and reproducible initial conditions for dry 3D channel models with hydrostatic or non-hydrostatic shallow-atmosphere equation sets. These can then be overlaid with a localized, unbalanced perturbation of e.g. the zonal wind field to initiate the growth of the baroclinic wave. Both an f- and β-plane configuration are described, which are anchored in the midlatitudes and have very similar temperature and static stability characteristics. The specification of the initial conditions is closely related to the initial data set derived for baroclinic wave studies with the dynamical cores of General Circulation Models (GCMs). These are documented in Jablonowski and Williamson (2006a,b) and Ullrich *et al.* (2014).

The initial conditions can serve many purposes. They can, for example, be used as a test case during the model development phases, and serve as a debugging tool or for numerical convergence studies. This was our original motivation for their derivation when we used them briefly for the evaluation of the new channel model MCore (Ullrich and Jablonowski 2012). However, the initial conditions can also serve as the basis for model intercomparisons, or investigations of the impact of the initial state on the baroclinic wave life cycle. The latter is the second focus area of this paper. The almost identical f- and β-plane configurations provide an opportunity to compare the different growth rates and most unstable wavelengths of the growing baroclinic waves. We provide example simulations with the models MCore and the Weather and Research Forecasting (WRF) model (Skamarock *et al.* 2008) and explain the simulation differences via linearized quasi-geostrophic (QG) theory. Of course, the underlying QG theory is well established, and this paper does not intend to broaden the theoretical base. Instead, we use the QG framework to validate the model results from a theoretical viewpoint, and demonstrate the close resemblance between the theory and the linear growth phases of the simulations. Having access to a closed-form analytical formulation of the initial conditions eases these QG assessments and closely connects all sections of the paper.

The paper is organized as follows. Section 2 provides an in-depth description of the initial data set for our baroclinic wave studies and outlines the generic "recipe" for the initialization technique. Section 3 specifies the recommended model configuration, briefly introduces the models MCore and WRF, and presents some example simulations on both the f- and β-plane. Section 4 shows how linearized QG theory can be used to validate the simulation results. The conclusions are summarized in section 5.

2. Initial conditions for a baroclinic wave in a channel

2.1. *Steady-state initial conditions*

The initial conditions for 3D baroclinic wave simulations have been designed for dry atmospheric channel models on a Cartesian plane. Both hydrostatic and non-hydrostatic equation sets with a shallow-atmosphere approximation are supported. The analytical formulation is based on a pressure-based vertical coordinate like the pure pressure coordinate p, the pure $\sigma = p/p_s$ coordinate (Phillips 1957) or the η (hybrid $\sigma - p$) coordinate (Simmons and Burridge 1981) with $p = A(\eta)p_0 + B(\eta)p_s$ (see detailed discussion in Appendix A). The reference surface pressure needs to be set to $p_0 = 1000$ hPa here. If other reference surface pressures are employed in a model, such as the sometimes used "standard atmosphere" of 1013.25 hPa, we recommend resetting the p_0 parameter to 1000 hPa to allow for comparisons to other published results. It is paramount that the initially constant surface pressure p_s is set to the same value $p_s = p_0$. This guarantees that the initial η surfaces coincide with constant σ or pressure surfaces. If other σ-systems like $\sigma = (p - p_t)/(p_s - p_t)$ are used (Kasahara 1974), the chosen pressure p_t at the top model interface should be set to zero.

In general, the choice of the vertical coordinate system is model dependent and therefore left to the modeling group, despite the fact that each vertical coordinate system implies different boundary conditions in the vertical direction. In essence, the boundary condition needs to ensure that the vertical velocity, as expressed in the transformed vertical coordinate, is zero at both the surface and the uppermost model interface level. In practice, these formulation differences have been found to be insignificant for the evolution of the baroclinic wave over short 15-20 day time periods. Typically, terrain-following σ or η vertical coordinates are used in hydrostatic General Circulation Models (GCMs) or hydrostatic-pressure-based (also known as mass-based, see Laprise (1992)) in non-hydrostatic models. In addition, non-hydrostatic models often utilize a height-based vertical coordinate, as further detailed below and in Appendix B.

The initial state is defined by analytical expressions in horizontally Cartesian (x, y, η) coordinates where $x \in [0, L_x]$ indicates the zonal direction, $y \in [0, L_y]$ represents the meridional

Table 1. A list of physical constants used in this document.

Constant	Description	Value
a	Radius of the Earth	6.371229×10^6 m
Ω	Angular velocity of the Earth	7.292×10^{-5} s^{-1}
g	Gravity	9.80616 m s^{-2}
c_p	Specific heat capacity of dry air at constant pressure	1004.5 J kg^{-1} K^{-1}
R_d	Gas constant for dry air	287.0 J kg^{-1} K^{-1}

Table 2. A list of parameters used in this document.

Constant	Description	Value
T_0	Reference temperature	288 K
Γ	Lapse rate	0.005 K m^{-1}
b	Nondimensional vertical width parameter	2
u_0	Reference zonal wind speed	35 m s^{-1}
u_p	Magnitude of the zonal wind perturbation	1 m s^{-1}
p_0	Reference surface pressure	1000 hPa
L_x	Zonal extent of the domain	40000 km
L_y	Meridional extent of the domain	6000 km
L_p	Width parameter for the perturbation	600 km
x_c	Zonal center position of the perturbation	2000 km
y_c	Meridional center position of the perturbation	2500 km
y_0	Meridional position of reference latitude	$L_y/2$
φ_0	Reference latitude	$\pi/4 = 45^\circ$ N
f_0	f-plane Coriolis parameter	$2\Omega \sin\varphi_0$
β_0	β-plane parameter	$2\Omega \cos\varphi_0\ a^{-1}$
Φ_s	Surface geopotential	0 m^2 s^{-2}
z_s	Surface elevation	0 m
δ	Initial divergence	0 s^{-1}
N_0	Approximate Brunt-Väisälä frequency at position φ_0	0.014 s^{-1}
T_s	Approximate vertically-averaged temperature at φ_0	260 K
H	Scale height	$H = R_d T_s g^{-1}$
p_{top}	Suggested maximum pressure position of the model top	20 hPa
z_{top}	Suggested minimum height position of the model top	30 km
Δz	Suggested maximum vertical grid spacing	1 km
$\Delta x, \Delta y$	Suggested horizontal grid spacing	100 km
Δy_w	Meridional width parameter for the inclusion of moisture	3200 km
η_w	η-based width parameter for the inclusion of moisture	0.3
q_0	Maximum specific humidity amplitude	0.018 kg kg^{-1}

direction and $\eta = p/p_s \in (0, 1]$ denotes the position in the vertical direction which is unity at the surface and approaches zero at the model top. The channel widths $L_x = 40000$ km and length $L_y = 6000$ km are selected in our specification which approximately correspond to the circumference of the Earth in the longitudinal x-direction along the equator and the meridional extent of the Northern Hemisphere in the y-direction. All physical constants and parameters used for the initial data are given in Tables 1 and 2. Modelers are encouraged to select the same physical constants and parameters to foster model intercomparisons.

The background flow field is comprised of a zonal jet in the northern midlatitudes that is in hydrostatic and geostrophic balance, enforces the thermal wind relationship, and is a steady-state solution to the shallow-atmosphere equation set. The background zonal wind u, as also specified in Ullrich and Jablonowski (2012), is defined as

$$u(x, y, \eta) = -u_0 \sin^2\left(\frac{\pi\, y}{L_y}\right) \ln\eta \exp\left\{-\left(\frac{\ln\eta}{b}\right)^2\right\}$$
$$= -u_0 \sin^2\left(\frac{\pi\, y}{L_y}\right) \ln\eta\ \eta^{\frac{-\ln\eta}{b^2}} \quad (1)$$

which forces the wind to be zero at the surface and along the north and south y-boundary. In addition, the wind approaches zero near the model top. The nondimensional vertical width parameter b is set to 2 and the default value of $u_0 = 35$ m s^{-1} is chosen. Note that the parameter u_0 does not indicate the maximum amplitude of the westerly zonal wind. The maximum is lower and lies around 30 m s^{-1} which resembles the zonal-mean time-mean jet speed in the midlatitudinal troposphere. The center of the zonal jet in the vertical direction is located around $\eta = 0.24$ or $p = 240$ hPa which is close to the observed position of midlatitudinal jets. As mentioned above, the zonal wind at the surface is zero. Therefore, the surface geopotential is constant and set to $\Phi_s = g z_s = 0$ m^2 s^{-2} which prescribes a flat surface elevation of $z_s = 0$ m. The physical constant $g = 9.80616$ m s^{-2} denotes the gravity.

The meridional wind v is set to zero. In addition, the vertical velocity w is set to zero for non-hydrostatic setups. This flow field is nondivergent ($\delta = 0$ s^{-1}) and even allows the derivation of the analytical initial conditions for models in vorticity-divergence (ζ,δ) form. The background relative vorticity field is given by

$$\zeta(x, y, \eta) = \frac{2\,\pi\, u_0}{L_y} \sin\left(\frac{\pi\, y}{L_y}\right) \cos\left(\frac{\pi\, y}{L_y}\right) \quad (2)$$
$$\times \ln\eta \exp\left\{-\left(\frac{\ln\eta}{b}\right)^2\right\}. \quad (3)$$

This leads to the expression for the absolute vorticity

$$\Omega_a(x, y, \eta) = f + \zeta(x, y, \eta) \quad (4)$$

where the Coriolis parameter f can be chosen to either represent a constant f-plane or β-plane. The two formulations are

$$f = f_0 \tag{5}$$
$$f = f_0 + \beta_0 \, (y - y_0) \tag{6}$$

with the constant Coriolis parameter $f_0 = 2\Omega \sin \varphi_0$ and the meridional variation of the Coriolis parameter $\beta_0 = 2\Omega \cos \varphi_0 \, a^{-1}$ at the constant latitude $\varphi_0 = 45^\circ$ N. The radius of the Earth is symbolized by $a = 6371.229 \times 10^3$ m, $\Omega = 7.292 \times 10^{-5}$ s^{-1} denotes the Earth's angular velocity and $y_0 = L_y/2$ is the center point of the domain in the y-direction. The steady-state zonal wind and relative vorticity field with respect to the vertical η coordinate are depicted in Fig. 1. They are identical for both the f- and β-plane formulation of the initial data set.

As the last step, we need expressions for the balanced geopotential and temperature fields. The geopotential is given by

$$\Phi(x,y,\eta) = \langle \, \Phi(\eta) \rangle + \Phi'(x,y) \; \ln \eta \, \exp \Big\{ - \Big(\frac{\ln \eta}{b} \Big)^2 \Big\} \tag{7}$$

with the horizontal-mean geopotential

$$\langle \Phi(\eta) \rangle = \frac{T_0 \, g}{\Gamma} \Big(1 - \eta^{\frac{R_d \, \Gamma}{g}} \Big) \tag{8}$$

and the horizontal variation

$$\begin{aligned} \Phi'(x,y) = \frac{u_0}{2} \Bigg\{ & \big(f_0 - \beta_0 y_0 \big) \Big[y - \frac{L_y}{2} - \frac{L_y}{2\,\pi} \sin \Big(\frac{2\pi y}{L_y} \Big) \Big] \\ & + \frac{\beta_0}{2} \Bigg[y^2 - \frac{L_y y}{\pi} \sin \Big(\frac{2\pi y}{L_y} \Big) \\ & - \frac{L_y^2}{2\,\pi^2} \cos \Big(\frac{2\pi y}{L_y} \Big) - \frac{L_y^2}{3} - \frac{L_y^2}{2\,\pi^2} \Bigg] \Bigg\}. \end{aligned} \tag{9}$$

The reference temperature T_0 is set to 288 K, the lapse rate is chosen as $\Gamma = 0.005$ K m^{-1} and $R_d = 287$ J kg^{-1} K^{-1} is the gas constant for dry air. The corresponding temperature distribution comprises the level-dependent horizontal-mean temperature $\langle T(\eta) \rangle$ and a horizontal temperature perturbation T'. They are given by

$$\begin{aligned} T(x,y,\eta) = & \langle \, T(\eta) \rangle \\ & + \frac{\Phi'(x,y)}{R_d} \left(\frac{2}{b^2} \, (\ln \eta)^2 - 1 \right) \exp \Big\{ - \Big(\frac{\ln \eta}{b} \Big)^2 \Big\} \end{aligned} \tag{10}$$

with the horizontal-mean temperature

$$\langle \, T(\eta) \rangle = T_0 \; \eta^{\frac{R_d \Gamma}{g}}. \tag{11}$$

This horizontal-mean temperature profile describes a linear temperature decrease with height, using a lapse rate of Γ. As mentioned above, the initial data enforce hydrostatic, geostrophic and thermal wind balance analytically. If a constant f-plane is desired the parameter β_0 can simply be set to zero which simplifies the initial conditions.

The initial temperature, geopotential height, potential temperature, absolute vorticity, Brunt-Väisälä frequency N and Ertel's PV on the constant f-plane are shown in Fig. 2. The corresponding initial data on the β-plane are presented in Fig. 3. Both plots depict the initial state with respect to the vertical η coordinate. The potential temperature patterns and N indicate that the initial data are statically stable. In addition, the absolute vorticity and PV distributions (positive on this northern hemispheric plane) fulfill the conditions for inertial and symmetric stability. However, the profiles are unstable with respect to barotropic and baroclinic instability mechanisms. Figure 3 demonstrates that the addition of the β-plane only leads to minor changes of the initial temperature and geopotential fields, and has very similar static stability characteristics.

The geopotential equation (7) is needed for 3D channel models with height-based vertical coordinates. Then an accurate root-finding algorithm is recommended to determine the corresponding η-level for any desired height position z. This iterative method, which is also applicable to isentropic vertical coordinates (Jablonowski and Williamson 2006a), is outlined in Appendix B. The manuscript supplement also shows the corresponding initial data with respect to the z coordinate. The latter two figures depict the meridional-vertical cross section of the pressure field instead of the geopotential height. Furthermore, this appendix lists the pressure, density and potential temperature equations that are typically needed for non-hydrostatic models.

In general, the complexity of the initial conditions can easily be extended to allow for a wide range of application areas. For example, the background zonal wind profile used here could be overlaid with a meridional zonal wind gradient to introduce either cyclonic or anticyclonic barotropic wind shear. Such modifications will impact the baroclinic wave life cycles as e.g. discussed by Davies *et al.* (1991), Thorncroft *et al.* (1993) or Davis (2010). Therefore, the description of the analytical initial state presented here can also be viewed as a generic recipe. This recipe closely follows the technique that was outlined for spherical geometry in the appendix of Jablonowski and Williamson (2006b). Once a zonally-symmetric background zonal wind field is analytically specified, and $v = w = 0$ m s^{-1} and $p_s = p_0$ are selected, the steady-state meridional momentum equation (written for a vertical pressure coordinate) can be integrated to yield the horizontal geopotential perturbation Φ'. The integration constant follows from the condition that the horizontal mean of Φ' must vanish. Utilizing the hydrostatic balance then gives the horizontal temperature pertubation T'. All that is left is the selection of the horizontal-mean background stratification $\langle \, T(\eta) \rangle$, which then yields the balanced mean geopotential $\langle \Phi(\eta) \rangle$ via the integration of the hydrostatic equation. The corresponding integration constant must ensure that the horizontal-mean $\langle \Phi_s(\eta) \rangle$ at the surface is zero. As a last step, the static stability of the new initial data needs to be assessed to guarantee that the chosen design and parameters lead to a statically stable configuration. If necessary, parameters like u_0 might need to be adjusted to yield $N^2 > 0$ s^{-2}. Note that a nonzero zonal wind at the surface will lead to a nonzero surface geopotential Φ_s and thereby a meridional variation of the surface elevation z_s.

These initial conditions are perfectly balanced in a continuous sense, and very well balanced balanced in the discrete system. If an even better discrete balance is desired, e.g. volume-mean values for finite-volume models, then Gaussian quadrature can be used to subsample the initial fields at the Gaussian quadrature points.

The initial conditions can also be easily extended to allow for simulations of idealized moist baroclinic waves as e.g. investigated by Tan *et al.* (2004), Waite and Snyder (2013) or Mirzaei *et al.* (2014). As before, none of these authors specify analytical conditions for their initial moisture fields. In addition, their prescribed initial relative humidity fields differ, and the balancing algorithms for the moist conditions are not thoroughly described. Appendix C provides the details of an analytical technique that adds specific humidity to the balanced initial fields.

2.2. *Baroclinic wave triggering mechanism*

A baroclinic wave can be triggered if the balanced zonal wind is overlaid with a localized perturbation. Here a zonal wind

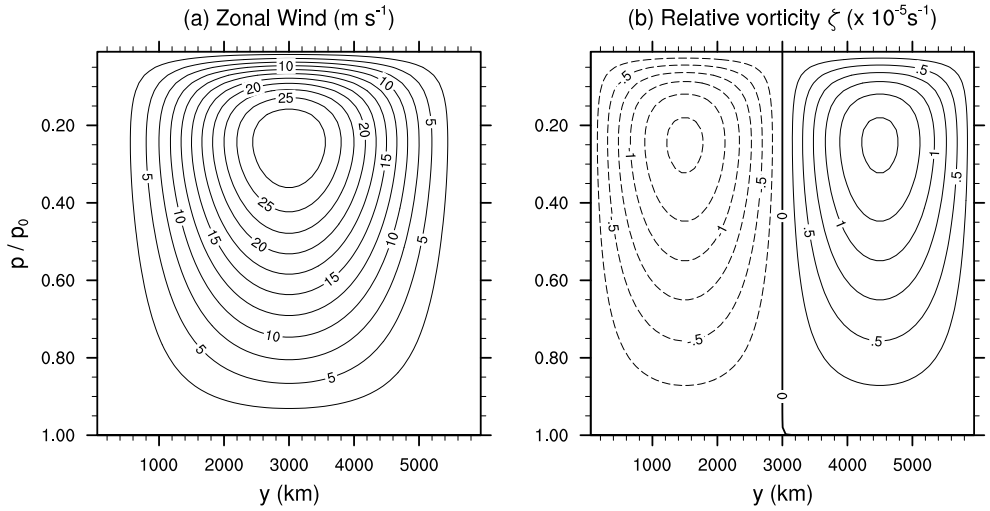

Figure 1. Meridional-vertical cross sections of the initial steady-state (a) zonal wind and (b) relative vorticity with respect to the η vertical coordinate. Negative contours are dashed.

perturbation u' with a Gaussian profile is centered at $(x_c, y_c) = (2000\text{ km}, 2500\text{ km})$ and given by

$$u'(x,y,\eta) = u_p \ \exp\left\{ -\left(\frac{(x-x_c)^2 + (y-y_c)^2}{L_p^2} \right) \right\} \quad (12)$$

with the width parameter $L_p = 600$ km and maximum amplitude $u_p = 1\text{ m s}^{-1}$. This perturbation is not balanced by the mean state and gets superimposed on the zonal wind field (1) by adding u' to u at each grid point at all model levels

$$u_{wave}(x,y,\eta) = u(x,y,\eta) + u'(x,y,\eta). \quad (13)$$

The zonal wind perturbation is depicted in Fig. 4. It covers a domain with a diameter of about 2500 km. As an aside, the unbalanced perturbation initially triggers high-speed gravity waves. They are apparent during the early stages and damped by diffusion over time before the growth of the baroclinic wave dominates the fluid flow.

If models employ the relative vorticity and divergence as prognostic variables, the corresponding perturbations are given by

$$\zeta'(x,y,\eta) = \frac{2\,(y-y_c)\,u'}{L_p^2} \quad (14)$$

$$\delta'(x,y,\eta) = \frac{-2\,(x-x_c)\,u'}{L_p^2}. \quad (15)$$

These then need to be added to the background ζ and δ fields.

2.3. *Boundary conditions for channel models*

Periodic boundary conditions are suggested for the x-direction. If such periodic conditions are not possible due to the model design the analytical initial state can be prescribed along the x-boundaries as long as the developing baroclinic wave does not approach the easternmost edge of the domain. This is not the case for short 15-day simulations when using the suggested parameter set with $u_0 = 35\text{ m s}^{-1}$. In case boundary issues arise the use of a zonal damping layer could be considered. Note that the channel width L_x can also be varied, even decreased, as long as the wave does not approach the x-edge. This does not change the character of the solution.

At the southern boundary $y = 0$ and northern boundary $y = L_y$ additional boundary conditions must be specified. Either no-flux or prescribed Dirichlet boundary conditions can be used, and either choice produces indistinguishable results. The following time-invariant Dirichlet boundary conditions in the y-direction have been used here:

$$p_s(x, y=0, t) = p_s(x, y=L_y, t) = p_0 \quad (16)$$

$$u(x, y=0, \eta, t) = u(x, y=L_y, \eta, t) = 0 \quad (17)$$

$$v(x, y=0, \eta, t) = v(x, y=L_y, \eta, t) = 0 \quad (18)$$

$$w(x, y=0, \eta, t) = w(x, y=L_y, \eta, t) = 0 \quad (19)$$

$$T(x, y=0, \eta, t) = T(x, y=0, \eta, t=0) \quad (20)$$

$$T(x, y=L_y, \eta, t) = T(x, y=L_y, \eta, t=0). \quad (21)$$

This formulation effectively prescribes the initial state along the y-boundaries. If the potential temperature Θ is used as the prognostic variable the temperature boundary condition can simply be converted to Θ. If boundary conditions are needed for the pressure p or density ρ, they are expressed in the same way as the boundary conditions for T. In our experiments we have not observed any negative boundary effects at the $y = 0$ or $y = L_y$ edges of the domain over the 15-day simulation period and recommend not using any sponge zones near the y-edges.

3. Selected configurations and numerical results

3.1. *Flow and model configurations*

The initial data can be used for numerical or physical science questions, both on a constant f- and β-plane. If the initial data are used as a test case to e.g. support the intercomparison of numerical schemes or to serve as a debugging tool during the model development phases, we recommend using the steady-state initial conditions without the zonal wind perturbation as the first step. This assesses how well and long the numerical discretization can maintain the initial steady-state which is the analytical solution. If possible the model should be run without explicit diffusion to minimize the degradation of the steady-state. The second more advanced configuration evaluates the evolution of a baroclinic wave in the Northern Hemisphere. It is triggered when using the steady-state initial conditions with the overlaid zonal wind perturbation. If applicable and needed, the model- and resolution-dependent subgrid-scale diffusion mechanisms with standard parameters should be used. All simulations should cover at least a 15-day time period.

If numerical convergence-with-resolution studies are desired we recommend using the horizontal grid spacings $\Delta x = \Delta y =$ 200 km, 100 km, 50 km and 25 km. If physical science questions are addressed, such as the impact of the varying Coriolis force on

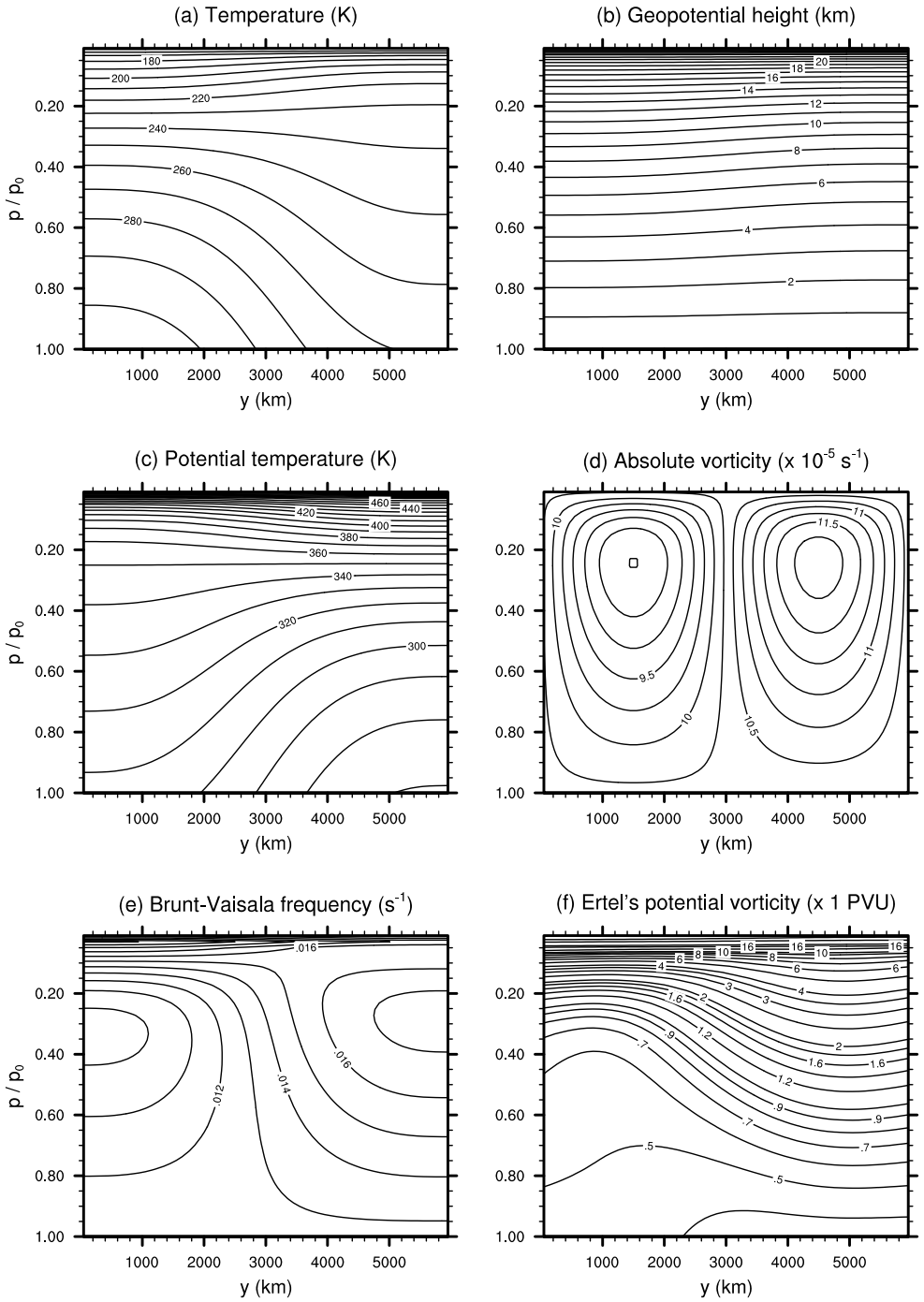

Figure 2. Meridional-vertical (η) cross sections of the steady-state initial conditions on a constant f-plane: (a) temperature, (b) geopotential height, (c) potential temperature, (d) absolute vorticity, (e) Brunt-Väisälä frequency N and (f) Ertel's PV with units PVU = 10^{-6} K m^2 kg^{-1} s^{-1}.

the evolution of a baroclinic wave as it is the focus in this paper, the horizontal grid spacing should be at least 100 km or finer. At this grid spacing solutions start to converge.

In the vertical direction, at least 30 levels with a suggested maximum grid spacing Δz = 1 km should be used. The model top should lie at or above the $p_{top} = 20$ hPa or $z_{top} = 30$ km position to capture the majority of the zonal jet structure in the upper atmosphere. A higher-altitude model top is even preferred, but adds extra computational cost. The type of vertical coordinate and the placement of the vertical levels should be documented. In addition, we recommend listing the time steps, dissipation mechanisms and their coefficients for all simulations to allow for straightforward comparisons with other published results. The baroclinic instability wave does not have an analytical solution. Therefore, high resolution ($\Delta x = \Delta y \leq 25$ km) reference solutions and their uncertainties need to be assessed for convergence studies. These suggestions closely follow the recommendations for the baroclinic wave test case in spherical geometry that is documented in Jablonowski and Williamson (2006a).

3.2. *Example models*

We pick two non-hydrostatic models to demonstrate the characteristics of the baroclinic wave. Both models produce comparable evolutions of the baroclinic instability, and therefore give confidence that our solutions are credible. In addition, this provides two points of comparison for other modelers. We do not conduct a thorough model intercomparison which is not the focus of this paper. Instead, we use these example results to draw attention to the interesting evolution paths of the baroclinic instability depending on the f- and β-plane approximations. This further motivates our theoretical investigations in section 4.

The two example models are the channel configuration of MCore (Ullrich and Jablonowski 2012) and WRF, version 3,

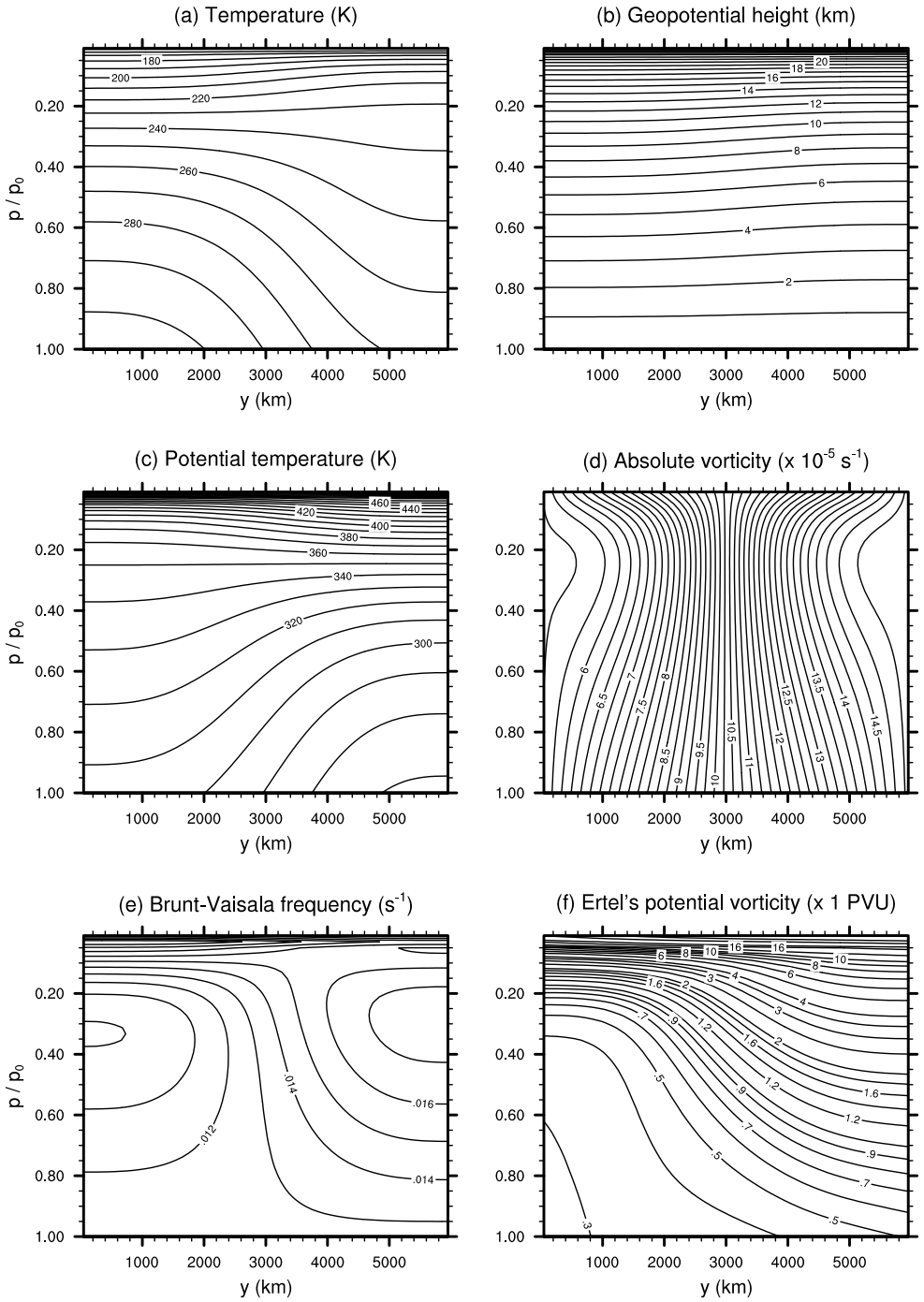

Figure 3. Meridional-vertical (η) cross sections of the steady-state initial conditions on the β-plane: (a) temperature, (b) geopotential height, (c) potential temperature, (d) absolute vorticity, (e) Brunt-Väisälä frequency N and (f) Ertel's PV with units PVU = 10^{-6} K m^2 kg^{-1} s^{-1}.

described in Skamarock *et al.* (2008). The latter has been developed at the National Center for Atmospheric Research (NCAR). In brief, both models use a finite-volume discretization and either a vertically-implicit (MCore) or split-explicit (WRF) time-split approach for handling the high-speed waves in the vertical direction. MCore utilizes a fourth-order spatial discretization on an unstaggered A-grid, whereas WRF's numerical scheme is second-order accurate and built upon a staggered C-grid. MCore employs a height-based vertical coordinate, whereas WRF is designed with the hydrostatic-pressure (mass-based) vertical coordinate. All experiments use identical horizontal grid spacings of $\Delta x = \Delta y = 100$ km. MCore is configured with 30 vertical levels that utilize an equidistant vertical grid spacing of $\Delta z = 1$ km (with the lowermost full model level position at $z = 500$ m) and a model top at $z_{top} = 30$ km. WRF is configured with 64 vertical levels with non-equidistant vertical grid spacings that are $\Delta z \approx 300$ m close to the ground (with the lowermost full model level position at $z \approx 150$ m). The spacing is stretched in the vertical direction, with the same model top at 30 km. The MCore time step is $\Delta t = 240$ s, WRF uses a time step of 600 s. MCore's diffusion mechanism is a flow-dependent implicit numerical diffusion which is part of its Riemann solver as explained in Ullrich and Jablonowski (2012). WRF's diffusion mechanisms are 3D divergence damping, an external mode filter and a time-offcentering technique for sound waves, which all use the standard coefficients documented in Skamarock *et al.* (2008). No Laplacian-type explicit diffusion or hyper-diffusion mechanisms are applied.

3.3. Snapshots of the baroclinic wave on the f- and β-plane

This section focuses on selected snapshots of the baroclinic wave on the f- and β-plane. Example results for the steady-state configuration and how it can be used for the assessment

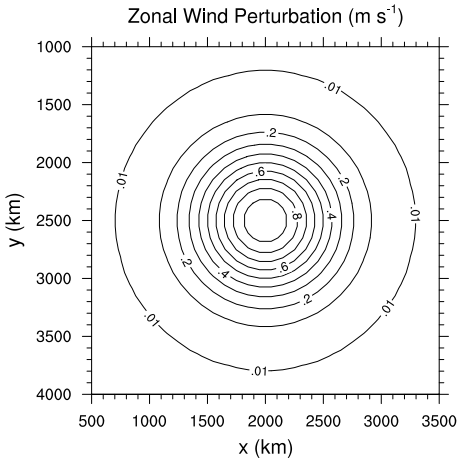

Figure 4. The vertically uniform zonal wind perturbation.

of the order of accuracy of a numerical scheme are shown in Ullrich and Jablonowski (2012) which numerically confirmed the theoretical fourth-order accuracy of the model MCore. We run the baroclinic wave simulations for 15 days to capture the initial and rapid development stages of the baroclinic disturbance. In general, the baroclinic wave starts growing noticeably after ≈ 6 days and evolves rapidly afterwards. Once the wave breaks, the flow enters a turbulent mixing stage.

Figures 5 and 6 display snapshots of the baroclinic waves that have been simulated on the f- and β-plane, respectively, with $u_0 = 35$ m s^{-1}. The β-plane formulation adds extra complexity to the simulation and gives insight into the effects of a varying Coriolis force. In particular, Fig. 5 shows the WRF (left) and MCore (right) f-plane 500 m pressure, temperature and relative vorticity at day 12. This vertical position is identical to the lowest model level in MCore, and requires vertical interpolations of the WRF data. The 500 m low-lying position is chosen since the baroclinic wave develops its strongest gradients close to the ground. Figure 6 shows the identical 500 m fields at day 10 as simulated with the β-plane variant of the initial conditions in WRF (left) and MCore (right). The baroclinic waves, although idealized, represent very realistic flow features in both Coriolis-term configurations and models. Strong temperature fronts develop that are associated with the evolving sequence of low and high pressure systems. The latter are also mirrored in the relative vorticity patterns with strong positive relative vorticity near the low pressure centers. The WRF and MCore results closely resemble each other which suggests that the flow patterns are trustworthy.

The growth rate of the wave strongly depends on the choice of the f- or β-plane approximation and the u_0 parameter. In our experiments, the 500 m temperature wave breaks around day 13.5 on the f-plane. In contrast, the 500 m temperature wave evolves more rapidly on the β-plane and breaks around day 11. In addition, the β-plane solution is confined to a narrower meridional width and exhibits a shorter wavelength of about 3300 km. The estimated wavelength of the $f-$plane simulation is about 4000 km. As an aside, if an alternative parameter $u_0 = 45$ m s^{-1} is utilized the atmosphere becomes even more baroclinic with increased vertical wind shear, and the evolution of the wave speeds up by about two days in both cases. We note that the MCore relative vorticity plots in Figs. 5(f) and 6(f) correct the relative vorticity plots shown in Ullrich and Jablonowski (2012) (their Figs. 12(c) and 13(c)) whose relative vorticity magnitudes were a factor of two too large.

Zonal-vertical cross sections of the flow from the MCore channel model at the location $y = L_y/2$ are shown in Fig. 7 for the f-plane at day 12 and in Fig. 8 for the β-plane at day 10. The figures depict the deviations of the geopotential, temperature, zonal velocity and meridional velocity from the balanced initial state which we define as "perturbations". Both the f- and β-plane geopotential perturbation and meridional wind show strong westward tilts with height. The temperature perturbations tilt eastward with height, especially in the lower atmosphere.

Note that the Froude numbers $Fr_h = U(LN)^{-1} \approx 2 \times 10^{-4}$ in the horizontal and $Fr_z = U(H_d N)^{-1} \approx 0.071$ in the vertical, as well as the Rossby number $Ro = U(Lf_0)^{-1} = 0.025$, of the flow are small ($\ll 1$) and thereby lie in the asymptotic regime of the QG theory. These assessments utilize the characteristic horizontal velocity scale of $U = 10$ m s^{-1}, the horizontal length scale of $L = 4000$ km of the baroclinic waves, the vertical depth scale of $H_d = 10$ km, the Brunt-Väisälä frequency $N = 0.014$ s^{-1}, and the Coriolis parameter $f_0 \approx 10^{-4}$ s^{-1} at 45° N. It means that the atmosphere is highly stratified and dominated by rotational effects which essentially confines the fluid to horizontal motions (Waite and Bartello 2006). This provides motivation to use theoretical concepts, like the linearized quasi-geostrophic (QG) theory, for further analysis and validation of the results in the next section. The remainder of the paper utilizes QG theory and the model MCore to analyze the differences between the f- and β-plane simulations.

4. Analysis

The dynamical behavior of the baroclinic instability is well understood in the context of linearized QG theory. The linear theory is valid only until the wave breaks, when non-linearities in the flow lead to mixing between wave modes. In this section we apply the known theory for the baroclinic instability to the flow configurations proposed in sections 2 and 3.1.

4.1. The baroclinic instability in a continuously stratified atmosphere

In order to analyze the evolution of the baroclinic instability we apply QG theory as e.g. detailed in Holton (2004). Here, we briefly summarize the most important QG aspects as they apply to our analyses of the f-plane and β-plane solutions. The linear QG theory typically utilizes log-pressure height coordinates, which are defined as

$$z^* = -H \ln\left(\frac{p}{p_0}\right), \tag{22}$$

where $p_0 = 1000$ hPa is the reference surface pressure, $H = R_d T_s g^{-1}$ is a standard scale height and T_s is an approximate vertically-averaged temperature at position $y_0 = 0.5 L_y$, chosen to be 260 K. The log-pressure height is roughly equivalent to a geometric height in the troposphere, although these profiles can diverge significantly in regions where the temperature does not match T_s. To analyze the stability of the baroclinic instability we define a geostrophic streamfunction

$$\psi \equiv \Phi / f_0, \tag{23}$$

so that the geostrophic wind can be expressed as $\mathbf{v}_\psi = \mathbf{k} \times \nabla\psi$. We further utilize the quasi-geostrophic potential vorticity q, defined in log-pressure coordinates as

$$q \equiv \nabla^2 \psi + f + \frac{1}{\rho_0} \frac{\partial}{\partial z^*} \left(\frac{f_0^2 \rho_0}{N^2} \frac{\partial \psi}{\partial z^*} \right). \tag{24}$$

Here, $\rho_0(z^*)$ is an approximate background density profile which is obtained analytically at the meridional center y_0 of the domain,

$$\rho_0(z^*) = \frac{p(z^*)}{R_d T\left(0, \frac{L_y}{2}, \eta(z^*)\right)}, \tag{25}$$

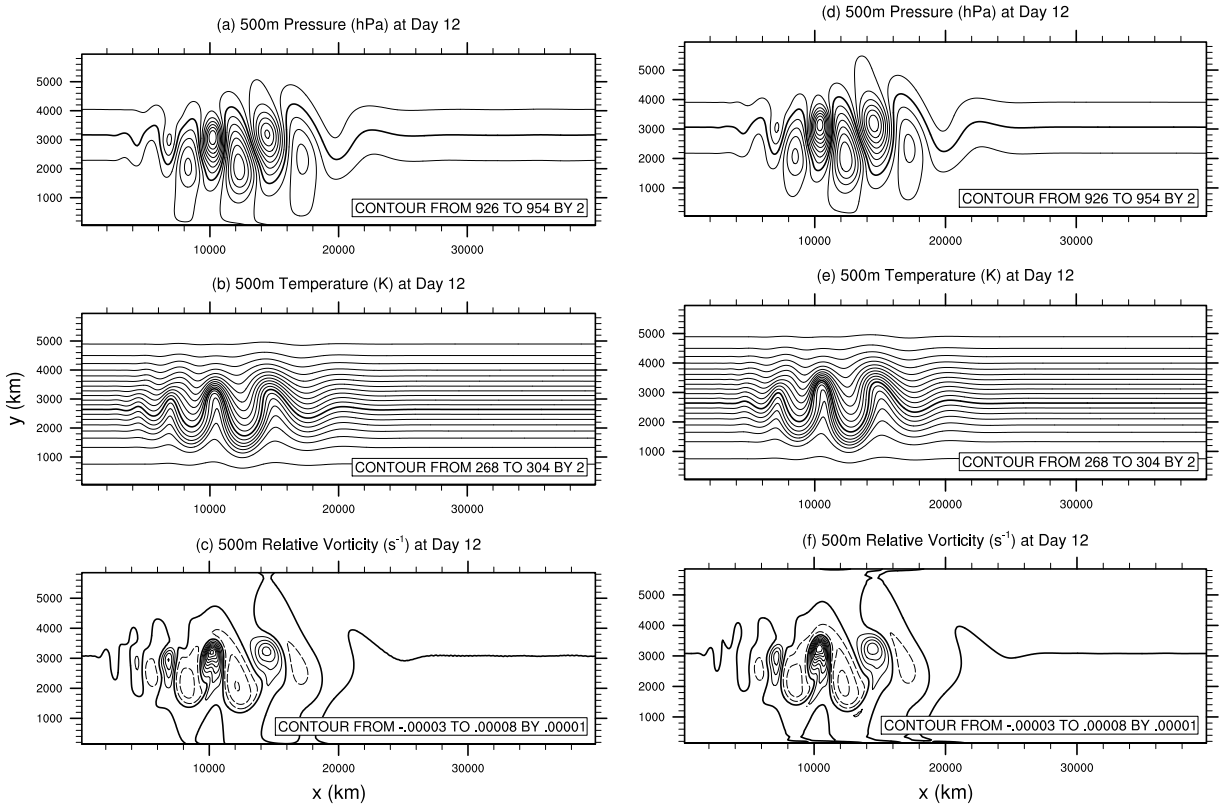

Figure 5. Horizontal $x-y$ cross sections of the baroclinic wave at day 12 on the f-plane as simulated by the (left, a-c) WRF and (right, d-f) MCore channel model. The plots show the (a,d) 500 m pressure field with enhanced 942 hPa contour line, (b,e) 500 m temperature with the coldest temperatures near $y = 0$ km and enhanced 290 K contour, (c,f) 500 m relative vorticity with enhanced zero contour.

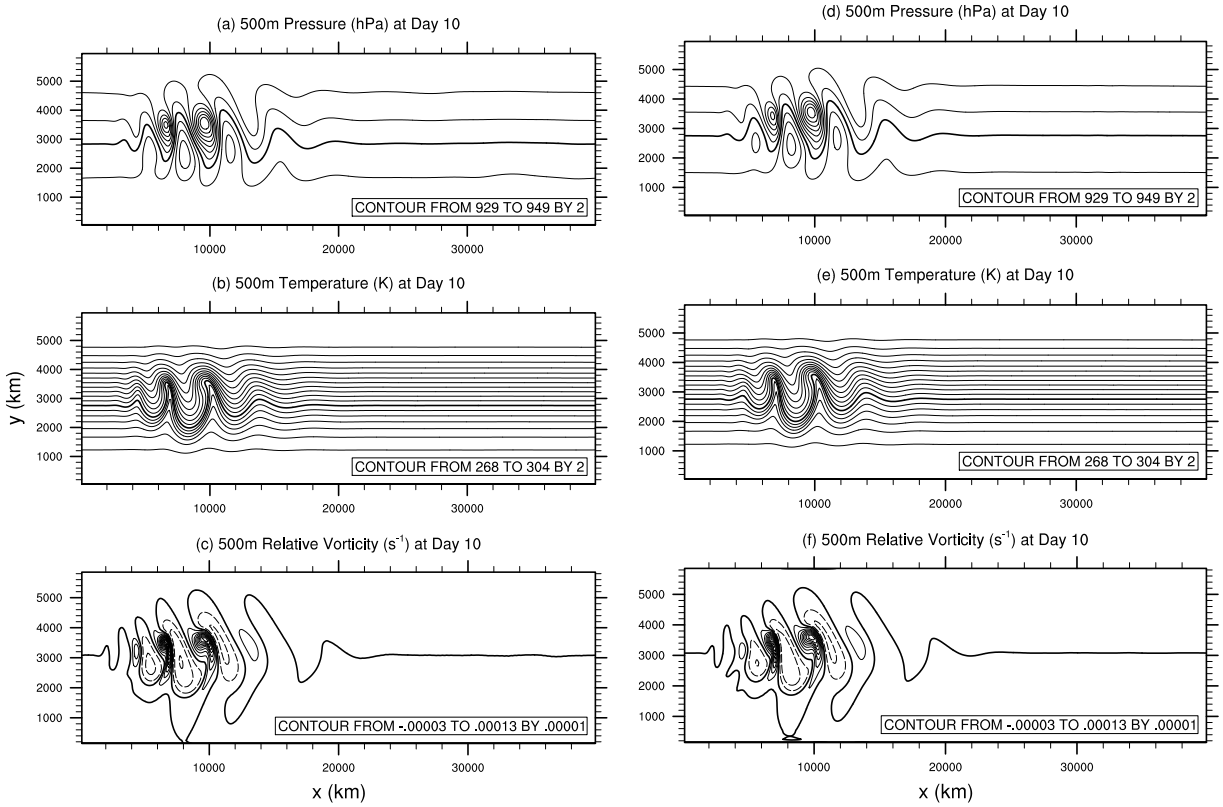

Figure 6. Horizontal $x-y$ cross sections of the baroclinic wave at day 10 on the β-plane as simulated by the (left, a-c) WRF and (right, d-f) MCore channel model. The plots show the (a,d) 500 m pressure field with enhanced 943 hPa contour line, (b,e) 500 m temperature with the coldest temperatures near $y = 0$ km and enhanced 290 K contour, (c,f) 500 m relative vorticity with enhanced zero contour.

using the temperature profile (10). The quasi-geostrophic potential vorticity equation and thermodynamic equation (for an adiabatic flow) can then be expressed in log-pressure coordinates as

$$\left(\frac{\partial}{\partial t} + \mathbf{v}_\psi \cdot \nabla\right) q = 0, \tag{26}$$

and

$$\left(\frac{\partial}{\partial t} + \mathbf{v}_\psi \cdot \nabla\right) \frac{\partial \Phi}{\partial z^*} + w^* N^2 = 0, \tag{27}$$

respectively. Here $w^* = Dz^*/Dt$ is the vertical velocity in log-pressure coordinates and t is time.

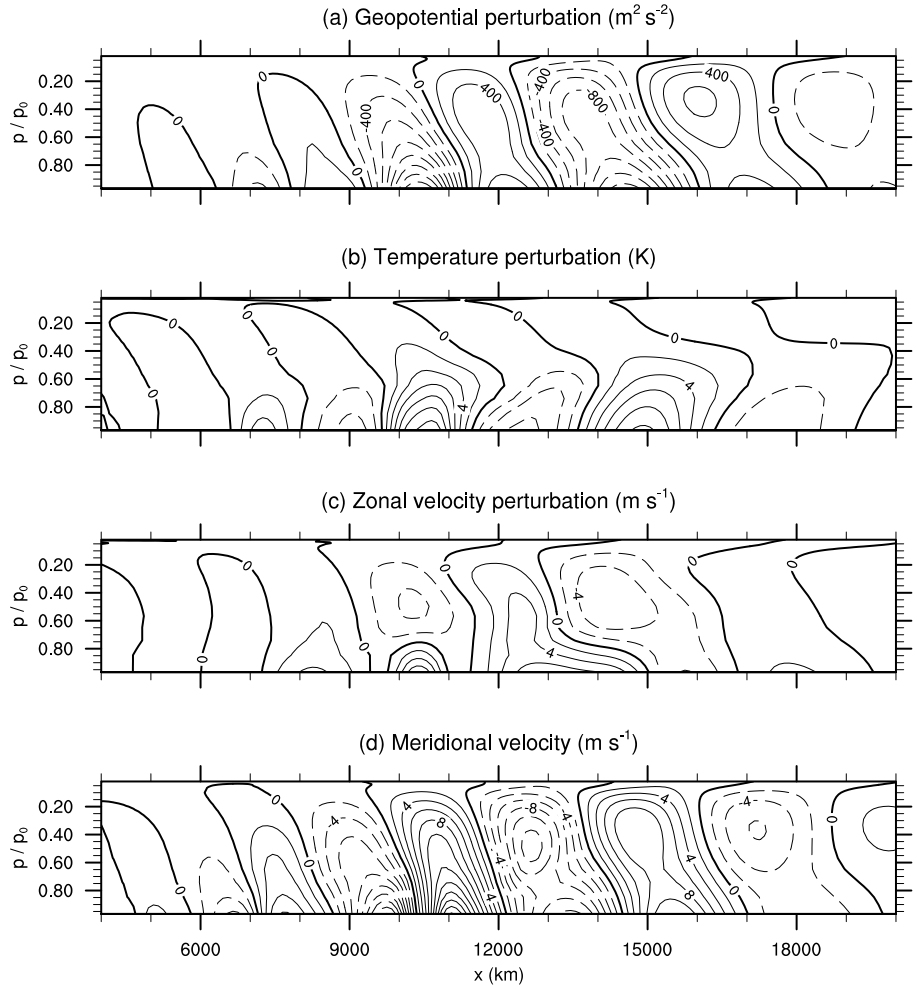

Figure 7. Zonal-vertical cross sections through $y = L_y/2$ of the baroclinic wave at day 12 on the f-plane as simulated by the MCore channel model. The plots show (a) geopotential (Φ) perturbation, (b) temperature perturbation, (c) zonal velocity perturbation and (d) meridional velocity. The contour spacing is (a) 200 m^2 s^{-2}, (b) 2 K, (c) 2 m s^{-1} and (d) 2 m s^{-1}. Dashed lines denote negative contours, the zero contour is enhanced.

The governing equations (26) and (27) are linearized using

$$q(x,y,z^*,t) = \overline{q}(y,z^*) + q'(x,y,z^*,t), \tag{28}$$
$$\psi(x,y,z^*,t) = \overline{\psi}(y,z^*) + \psi'(x,y,z^*,t), \tag{29}$$

where the overline denotes a zonally- and time-averaged mean state, and the prime symbolizes the deviations from the mean basic state. This leads to the linearized potential vorticity equation

$$\left(\frac{\partial}{\partial t} + \overline{u}\frac{\partial}{\partial x}\right) q' + \frac{\partial \overline{q}}{\partial y}\frac{\partial \psi'}{\partial x} = 0, \tag{30}$$

with

$$q' = \nabla^2 \psi' + \frac{1}{\rho_0}\frac{\partial}{\partial z^*}\left(\frac{f_0^2 \rho_0}{N_0^2}\frac{\partial \psi'}{\partial z^*}\right) \tag{31}$$

and

$$\frac{\partial \overline{q}}{\partial y} = \beta - \frac{\partial^2 \overline{u}}{\partial y^2} - \frac{1}{\rho_0}\frac{\partial}{\partial z^*}\left(\frac{f_0^2 \rho_0}{N_0^2}\frac{\partial \overline{u}}{\partial z^*}\right). \tag{32}$$

The constant Brunt-Väisälä frequency $N_0 = 0.014\ \mathrm{s}^{-1}$ represents an average near the meridional center y_0 in the region of greatest instability which lies between the surface and $\eta \approx 0.25$ (see also Figs. 2(e) and 3(e)). The balanced initial condition for u (Eq. (1)) serves as the mean background wind $\overline{u}(y, z^*)$.

The linearized thermodynamic equation (27) is applied at the top and bottom boundaries of the domain (the top boundary is assumed to be a rigid lid) where $w^* = 0$, so that it takes the form

$$\left(\frac{\partial}{\partial t} + \overline{u}\frac{\partial}{\partial x}\right)\frac{\partial \psi'}{\partial z^*} - \frac{\partial \psi'}{\partial x}\frac{\partial \overline{u}}{\partial z^*} = 0. \tag{33}$$

No-flux boundary conditions are applied at the meridional edges of the domain, which leads to the additional condition

$$\frac{\partial \psi'}{\partial x} = 0 \quad \Longrightarrow \quad \psi' = 0, \qquad \text{at } y = 0 \text{ and } y = L_y. \tag{34}$$

The perturbation streamfunction is assumed to consist of a single zonal Fourier component propagating zonally

$$\psi'(x,y,z^*,t) = \mathrm{Re}\left\{\Psi(y,z^*)\exp\left[ik(x-ct)\right]\right\}, \tag{35}$$

where Re denotes the real part of the equation, $\Psi = \Psi_r + i\Psi_i$ is the complex amplitude function, $c = c_r + ic_i$ is the complex phase speed, i symbolizes the imaginary unit, and k is the zonal wave number

$$k = \frac{2\pi \tilde{k}}{L_x}, \tag{36}$$

with the non-negative integer $\tilde{k} \in \{0, 1, 2, \ldots\}$. It denotes the number of cycles of the Fourier mode over the zonal domain. It then follows from (30) and (35) that

$$(\overline{u} - c)\left[\frac{\partial^2 \Psi}{\partial y^2} - k^2 \Psi + \frac{1}{\rho_0}\frac{\partial}{\partial z^*}\left(\frac{f_0^2 \rho_0}{N^2}\frac{\partial \Psi}{\partial z^*}\right)\right] + \frac{\partial \overline{q}}{\partial y}\Psi = 0, \tag{37}$$

which is an elliptic partial differential equation for Ψ in $(y, z) \in [0, L_y] \times [0, z^*_{top}]$. Boundary conditions in the meridional direction are given by (34), and at $z = 0, z^*_{top}$ by (33) and (35),

$$(\overline{u} - c)\frac{\partial \Psi}{\partial z^*} - \frac{\partial \overline{u}}{\partial z^*}\Psi = 0. \tag{38}$$

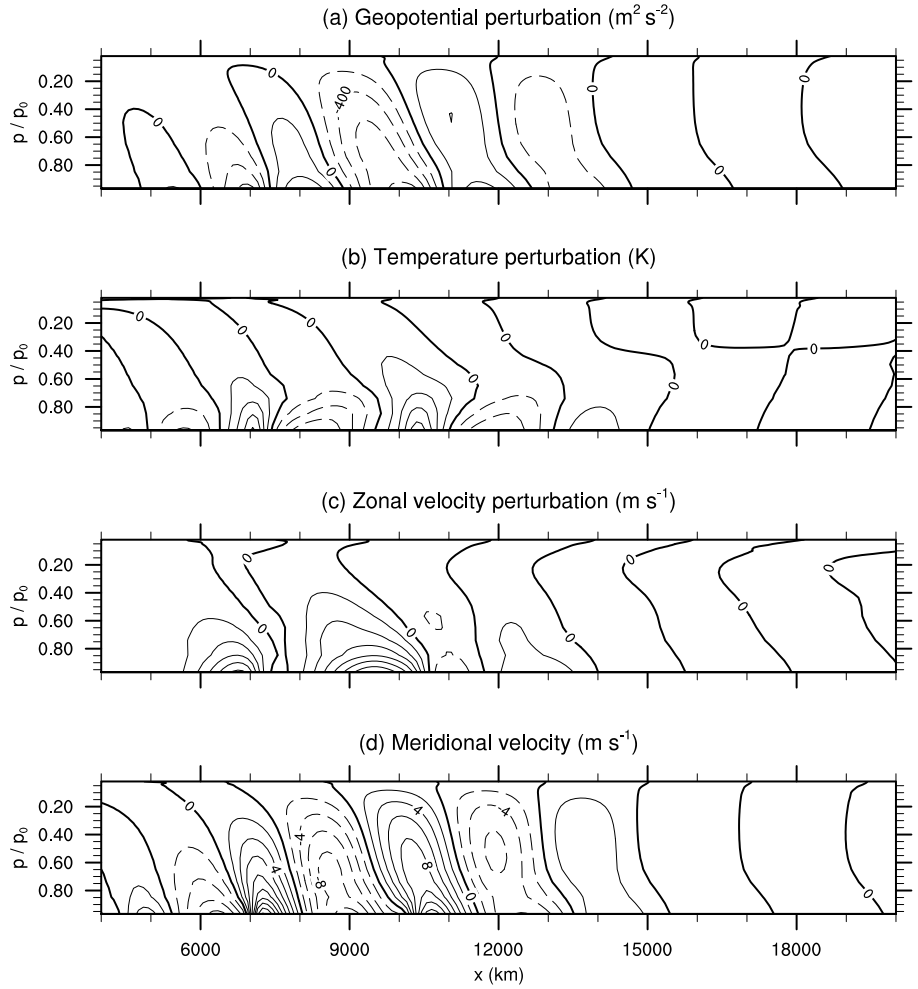

Figure 8. Zonal-vertical cross sections through $y = L_y/2$ of the baroclinic wave at day 10 on the β-plane as simulated by the MCore channel model. The plots show (a) geopotential (Φ) perturbation, (b) temperature perturbation, (c) zonal velocity perturbation and (d) meridional velocity. The contour spacing is (a) 200 m^2 s^{-2}, (b) 2 K, (c) 2 m s^{-1} and (d) 2 m s^{-1}. Dashed denote negative contours, the zero contour is enhanced.

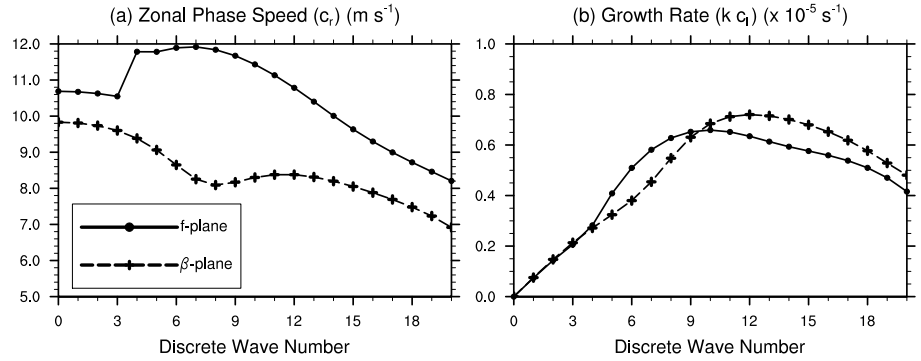

Figure 9. (a) Real phase speed and (b) growth rates of the streamfunction wave from QG theory for the discrete wave number range $\tilde{k}$ between $0 - 20$.

Since the phase speed c is unknown, we must solve a Sturm-Liouville (or boundary value) problem to find non-trivial solutions of (37)-(38) for eigenvalue / eigenfunction pairs $(c, \Psi(y, z^*))$.

Analytical solutions of the boundary value problem are difficult or impossible to obtain in general, and consequently we rely on a numerical solution. Our numerical approach is described in detail in Appendix D. To quickly summarize, we discretize (37)-(38) using standard second-order finite-difference operators, so that the Sturm-Liouville problem can be rewritten as an eigenvalue problem of the form

$$\mathsf{F}(k)\boldsymbol{\Psi}_d = c\boldsymbol{\Psi}_d, \tag{39}$$

where $\boldsymbol{\Psi}_d$ is a vectorized approximation to Ψ at each of the mesh nodes and $\mathsf{F}(k)$ is a discrete matrix operator which is dependent on the horizontal wave number. The resulting eigenvalue problem is then solved using the `eig` command in Matlab, which yields all discrete pairs $(c, \boldsymbol{\Psi}_d)$ that satisfy (39).

4.2. *Most unstable modes*

The non-trivial wave solutions (35) of the boundary value problem can also be expressed in the form

$$\psi'(x, y, z^*, t) = \exp(kc_i t)\ \mathrm{Re}\big\{\Psi(y, z^*)\exp\left[ik(x - c_r t)\right]\big\} \tag{40}$$

$$= \exp(kc_i t)\ \Psi_r \cos\left[k(x - c_r t)\right] - \exp(kc_i t)\ \Psi_i \sin\left[k(x - c_r t)\right] \tag{41}$$

Consequently, solutions with positive imaginary component $c_i > 0$ will cause the baroclinic instability to intensify over time.

The streamfunction wave mode with maximum growth rate $\alpha = kc_i$ will become dominant as $t \to \infty$, and so is referred to

as the *most unstable wave mode*. In Fig. 9 we plot the zonal phase speed c_r and growth rate kc_i for the discrete wave number range $\tilde{k}$ between $0-20$. Figure 9(b) shows that the most unstable modes (the maxima) as derived via QG theory occur at the discrete wave number $\tilde{k}=10$ on the f-plane, with $kc_i \approx 6.59 \times 10^{-6}$ s^{-1}, and at $\tilde{k}=12$ on the β-plane, with $kc_i \approx 7.21 \times 10^{-6}$ s^{-1}. This corresponds to a wavelength of roughly 4000 km on the f-plane and 3333 km on the β-plane. As displayed in Fig. 9(a) the zonal phase speed of this mode is 11.43 m s^{-1} on the f-plane and 8.38 m s^{-1} on the β-plane, which is significantly slower than the maximum zonal background flow $\overline{u}$ with ≈ 30 m s^{-1} in the upper atmosphere.

Besides the most unstable wave modes $\tilde{k}=10$ ($f-$plane) and $\tilde{k}=12$ ($\beta-$plane) displayed in Fig. 9b there are also neighboring wave numbers that grow at comparable rates. On the $f-$plane these range from wave numbers 8–12, on the $\beta-$plane these range from wave numbers 10–14. This aspect can lead to sensitivities in numerical solutions when asymmetric meshes are used, such as triangular or hexagonal grids. For example, the barotropic instability wave test case by Galewsky *et al.* (2004) exposes such sensitivities in the 2D shallow-water framework. Wave modes with similar growth rates were found to be impacted by grid inhomogeneities, especially at low resolutions with grid spacings > 120 km, which can lead to rather different evolutions of the growing instability wave. Examples are e.g. displayed in St-Cyr *et al.* (2008) and Weller *et al.* (2012) who showed that the growth of the Galewsky *et al.* (2004) barotropic instability wave on the sphere can be overshadowed by the growth of numerical discretization errors that originate from non-Cartesian grids. Evaluating such potential grid imprinting signatures in 3D channel models is therefore another application area of the initial conditions presented here.

We highlight that the QG growth rate of the most unstable mode on the β-plane is significantly larger than the growth rate on the f-plane. The higher growth rate and the shorter wavelength on the β-plane confirm our numerical findings from section 3.3. Interestingly, this QG result derived via the continuous equations seem to be partly contrary to results from the two-layer QG baroclinic wave theory (see, for example, Holton (2004) Section 8.2), which hold that the addition of a β term introduces a stabilizing effect to a baroclinic instability. However, we do note that the theoretical growth rate from the β-plane is smaller for longer waves ($\tilde{k}<10$) in agreement with the two-layer theory.

In Fig. 10 we plot the meridional-vertical cross sections of the real and imaginary components of the amplitude function Ψ for the most unstable wave modes on the f- and β-plane. Equation (41) explains how the real Ψ_r and imaginary Ψ_i components impact the pattern of the baroclinic wave. Their relative magnitudes determine the phase of the wave for any position (y, z^*).

Some example wave perturbations are shown in Figs. 11 and 12. The figures depict the zonal-vertical cross sections of the geopotential perturbation $\Phi' = \psi' f_0$, the temperature perturbation and the vertical pressure velocity $\omega = -w^* p H^{-1}$ along the center position y_0 on the f- and β-plane for their most unstable wave modes $\tilde{k}=10$ and $\tilde{k}=12$, respectively. Here, we are only interested in the general patterns of the QG wave perturbations in the (x, z^*) domain and leave out the secondary information about the actual amplitudes. The QG figures 11 and 12 confirm the WRF and MCore simulation results from section 3.3 (Figs. 7 and 8). Both the f- and β-plane perturbations of the QG geopotential and temperature fields agree well with the patterns of strongest development obtained from the simulations. In our QG analysis (Figs. 11 and 12) the geopotential perturbations are inclined westwards with altitude, whereas the temperature shows a dominant eastward tilt with height, especially in the lower atmosphere. These patterns are also present in WRF and MCore. In addition, we observe in the QG results that the updraft regions ($\omega < 0$ Pa s^{-1}) are co-located with warm temperature anomalies, and both the updraft and warm regions are located in-between the low (to the west) and high (to the east) geopotential perturbations.

4.3. *Power spectrum of the baroclinic instability*

In order to better understand how well the linear QG theory represents the flow field, we now evaluate the wave-like nature of the baroclinic instability. In Fig. 13 the zonal power spectrum of the MCore meridional velocity field is plotted at the center position y_0 at the lowest model level (500 m) on both the f- and β-plane. A 15-day simulation time period is depicted that displays the $\log_{10}$ power amplitudes for the discrete wave numbers $\tilde{k}$. The meridional velocity is directly connected to the geopotential perturbations via the geostrophic wind relationship. Since v is zero in the background the meridional velocity only picks out the power of the growing disturbance, and is therefore an ideal candidate for the analysis. Figure 13 shows that the discrete wave number $\tilde{k}=10$ on the f-plane and $\tilde{k}=12$ on the β-plane experience the biggest power amplitudes and therefore the most rapid growth in MCore. This growth process is dominated by linear interactions until wave breaking occurs. Once wave breaking sets in, deposition occurs into smaller scales, as observed around day 13.5 on the f-plane and around day 11 on the β-plane. Due to the nature of the non-linear interaction between wave modes, the system then sets up a series of resonances which inhibits the growth of certain discrete wave modes. This result is apparent in the Fourier spectra in Fig. 13, especially on the β-plane, where gaps are clearly present in the power spectrum after day 9.

To assess whether the linear QG theory validates the growth rate of the most unstable mode in MCore, Fig. 14 plots the amplitude versus time of the zonal Fourier power spectrum of the MCore meridional velocity at $\tilde{k}=10$ (f-plane, left) and $\tilde{k}=12$ (β-plane, right). The overlaid theoretical growth rate in Fig. 14 is assessed using kc_i from Fig. 9b. As shown in Eq. (41) the growth of the unstable wave is proportional to the exponential form $\exp(kc_i t)$. Note that Fig. 14 selects an arbitrary starting position (at $t=0$ s) for the theoretical growth rate which lies in close proximity to the MCore growth curve. This draws attention to the steepness of the two slopes which is the important piece of information here. Since the vertical axis is logarithmic, an exponential growth appears as a straight line. Figure 14 highlights the impressive agreement between the predicted growth rate from the linear QG theory and the growth rate obtained from the MCore simulation in the "linear regime" prior to wave breaking. The reason for the different modeled and theoretical slopes during the early phases is that a variety of growing wave modes with similar power are present in MCore before the most unstable wave mode dominates. After the wave has broken there is a clear loss of power associated with a transfer to finer scales, and consequently a deviation from the theoretically predicted growth rate. This also marks the time that is associated with enhanced gravity wave activity due to the nonlinear breaking of the baroclinic wave.

4.4. *Theoretical considerations*

In this section, we discuss the connection of our analysis to the theory of baroclinic instability. Notably, it is interesting that the most unstable wave modes for f- and β-plane configurations (Figures 11,12) are in rough qualitative agreement with the most unstable mode of the Eady model (Eady 1949), which is even more idealized than our QG analysis (see also textbooks like Holton (2004) or Vallis (2006)). The maximum vertical velocity occurs at roughly $\eta = 0.4$ ($z^* = 7$ km) in both cases, below the

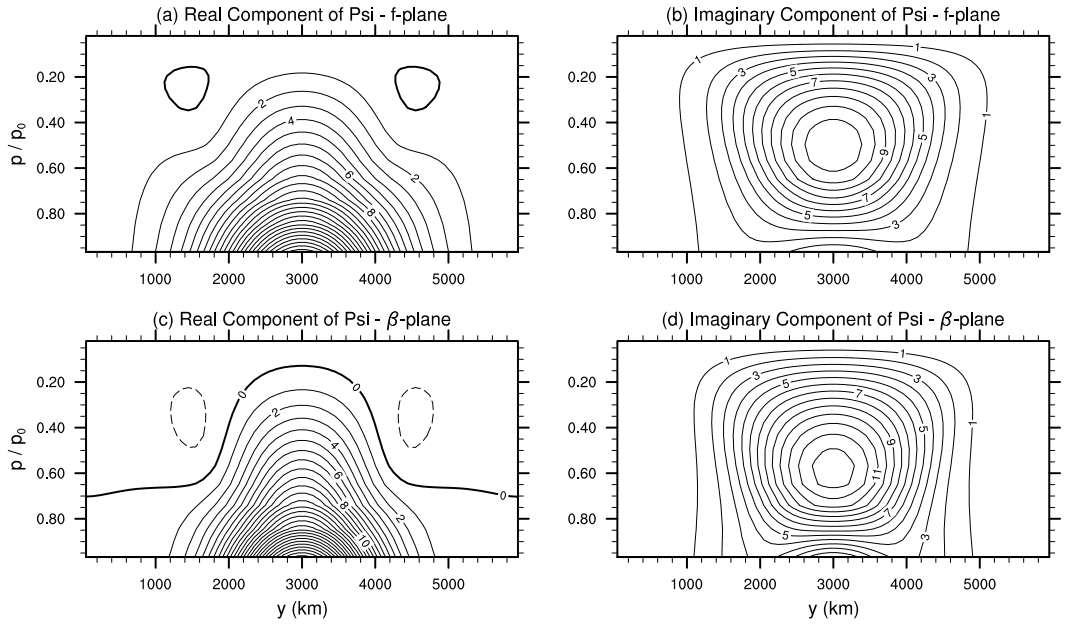

Figure 10. Meridional-vertical cross sections of the (a,c) real and (b,d) imaginary components of the streamfunction amplitude function $\Psi(y, z^*)$ for the most unstable wave mode (a,b) $\tilde{k} = 10$ on the f-plane and (c,d) $\tilde{k} = 12$ on the β-plane. Negative contours are dashed. The units are $\mathrm{m}^2\ \mathrm{s}^{-1}$.

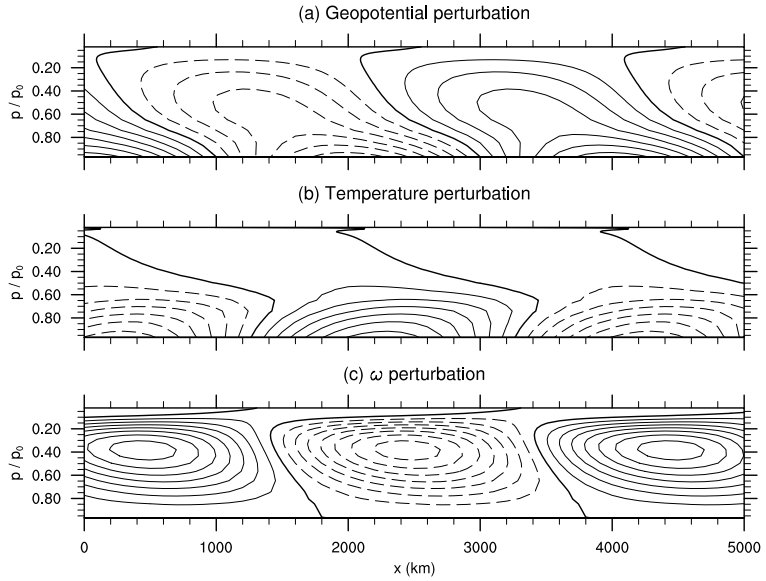

Figure 11. Zonal-vertical cross sections at the center position y_0 of the (a) geopotential, (b) temperature and (c) vertical pressure velocity perturbations for the most unstable mode $\tilde{k} = 10$ on the f-plane. Negative contours are dashed and the zero line is enhanced.

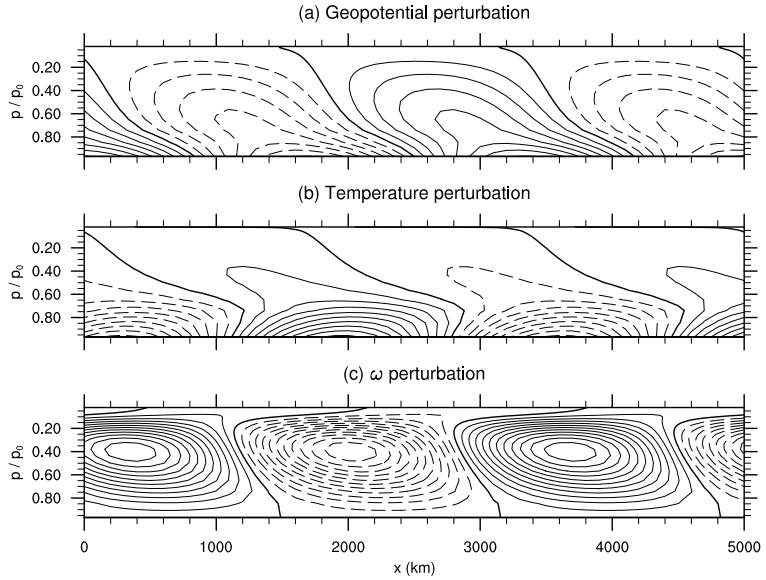

Figure 12. Zonal-vertical cross sections at the center position y_0 of the (a) geopotential, (b) temperature and (c) vertical pressure velocity perturbations for the most unstable mode $\tilde{k} = 12$ on the β-plane. Negative contours are dashed and the zero line is enhanced.

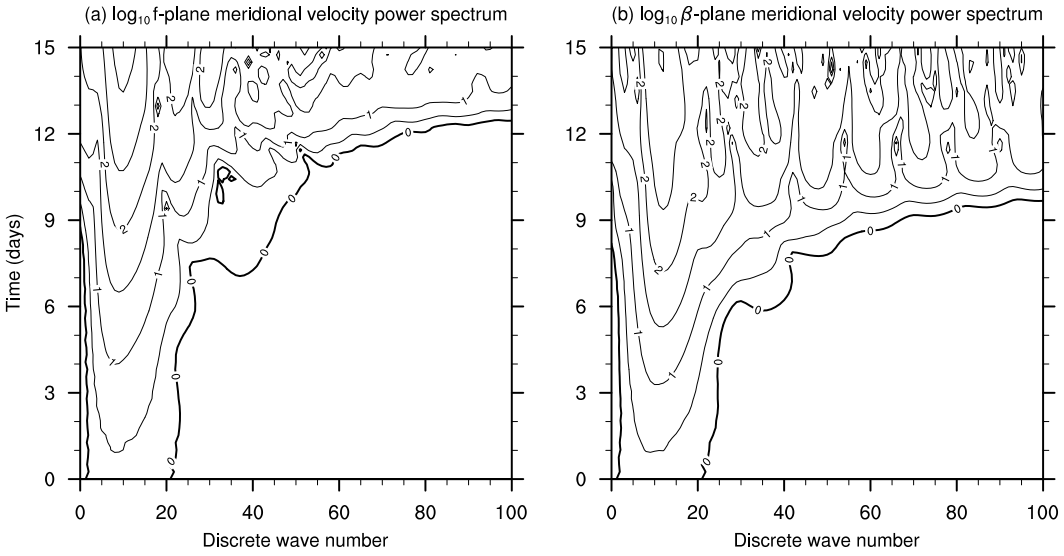

Figure 13. Dependence of the zonal Fourier power spectrum of the MCore meridional velocity at the center position y_0 and lowest model level (500 m) on the discrete wave numbers $\tilde{k}$. The contours show the $\log_{10}$ of the power spectra on the (a) f-plane and (b) β-plane over the 15-day simulation period.

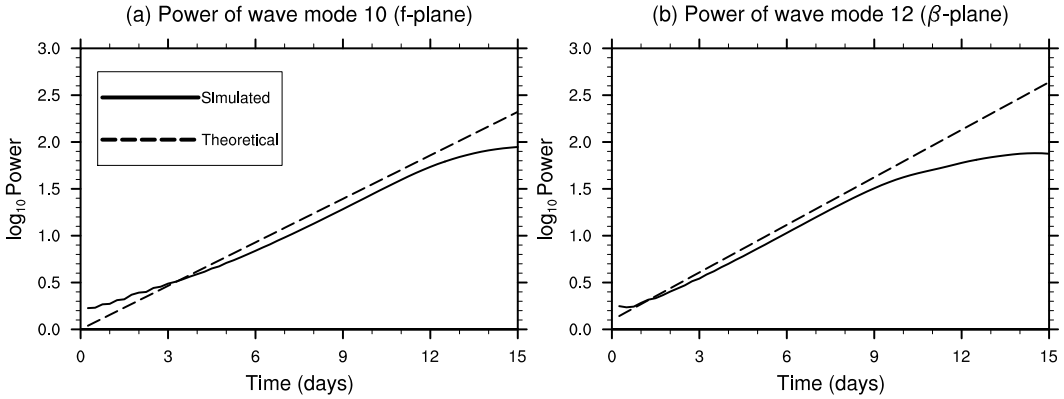

Figure 14. Power amplitude of the most unstable wave modes (a) $\tilde{k} = 10$ on the f-plane and (b) $\tilde{k} = 12$ on the β-plane over a 15-day simulation. The solid line shows the $\log_{10}$ of the zonal Fourier power spectrum of the MCore meridional velocity from Fig. 13. The theoretically predicted maximum growth rate, as derived from the linear QG theory, is shown by the dashed line.

upper atmospheric center position of the zonal jet (see Figures 7 and 8). The Eady model makes use of a rigid lid that assists the generation of the instability via so-called edge waves that propagate along the surface and rigid lid. However, the instability generated in our case is not sensitive to the altitude of the model top (above at least 20 km), and it is apparent that the unstable modes do not exhibit the vertical symmetry present in the Eady model. Further, the Eady model is known for a short wave cut-off which suppresses instability at the highest wavenumbers, whereas these simulations appear to exhibit no such cut-off (see Figure 9). This may suggest that the test case in this paper is more closely connected with the Charney model (Charney 1947) (which has no cut-off), and inspection of Figure 2 reveals that our initial conditions exhibit an internal PV gradient – whose strength varies between the f and β cases – which is absent in the Eady formulation.

In fact, the most rigorous theory describing the behavior of baroclinic instability is derived by Heifetz *et al.* (2004a), using counter-propagating Rossby-waves (CRWs) – that is, upper and lower wave modes whose counter-propagation relative to the mean flow leads to resonant growth. The theory builds on earlier work by Bretherton (1966), who extended Eady's 2-layer model to include a QG PV gradient and showed this framework could be used to capture the basic nature of the instability. Note that the QG theory itself does not apply directly to our initialization, since the stability parameter σ that appears in QG theory has significant variation in the y direction when computed from (1)-(11). Nonetheless, over short time scales, when the horizontal gradient of σ is perpendicular to the geostrophic wind, the QG theory will hold approximately. Using a spatially variable σ parameter, the meridional gradient of QG PV changes sign from negative in the lower model levels to positive in the upper model levels (not shown). The CRW theory notes that unstable baroclinic modes in the Eady model are only supported due to the boundaries, whereas in the Charney model these modes can exist due to the presence of an interior PV gradient (Heifetz *et al.* 2004b). The applicability of the CRW theory to our results is apparent when comparing (our) Figure 10 with Methven *et al.* (2005) Figure 3 and (our) Figures 7d, 8d with Methven *et al.* (2005) Figure 4e. Namely, it is apparent that Figure 10 actually shows the structure of the lower and upper CRWs associated with the prescribed background state, and exhibits westward-tilted behavior consistent with the CRW theory.

5. Conclusions

In this paper we have introduced idealized initial conditions for the simulation of baroclinic instability waves in 3D atmospheric channel models. The unique aspect of the initial conditions is that they are analytical for both an f- and β-plane configuration with only very minor differences in the initial states. The initial conditions and the evolving baroclinic waves are qualitatively very similar to those of a real atmosphere, which makes the initial state appealing for both numerical and physical science investigations.

First, the initial conditions can be considered a "baroclinic wave test case" to assess the numerical characteristics of 3D Cartesian

channel models. In particular, a steady-state configuration can be used as a first step for numerical convergence studies, before selecting the baroclinic wave configuration as a debugging or model intercomparison tool. Channel models are typically part of the model development hierarchy that consists of 2D ($x-y$) shallow water, 2D ($x-z$) Cartesian channel, 3D Cartesian channel and 3D dynamical cores on the sphere. A variety of nontrivial (non-isothermal, non-state-at-rest) test cases with analytical initial conditions exist in the literature for all model categories except for 3D Cartesian channel models. The only exception is the work by Staniforth (2012) who proposed exact stationary solutions of the Euler equations on $\beta-\gamma$ planes. In addition, Wang and Polvani (2011) provided a complete description of their balanced initial data sets on the f-plane which only require very basic numerical integrations, but more complex iterations to obtain the normal-mode perturbation. The typical assessments of baroclinic instability flows in 3D channels are based on initial data that heavily rely on numerical techniques for the PV inversion. Since these techniques are generally not fully documented, the results cannot be reproduced by others. Our approach guarantees reproducibility and helps fill this crucial gap. In addition, we provide a "recipe" on how to generate other analytical initial conditions, with e.g. additional meridional zonal wind shear or moisture (see Appendix C), to broaden the range of science questions. In order to provide examples of the flow field, we compared the evolution of the baroclinic wave in the two non-hydrostatic channel models MCore (Ullrich and Jablonowski 2012) and WRF (Skamarock *et al.* 2008). The baroclinic waves closely resembled each other, which suggests that the numerical solutions are trustworthy and provide a point of comparison for other modelers.

Second, the initial conditions also lay the groundwork for interesting physical science questions, such as the impact of the varying f- and β-plane Coriolis parameter on the flow field, which is a central point of this paper. Our f- and β-plane simulations use very similar initial data fields with identical vertical wind shear and almost identical static stability. These are factors that are known for their impact on the growth of unstable baroclinic waves. The numerical experiments showed that the evolution of the baroclinic wave on the β-plane is more unstable than the corresponding f-plane configuration, experiencing a faster linear growth rate of the most unstable wave mode, a shorter most unstable wavelength, a narrower meridional width, and an earlier breaking of the baroclinic wave. A theoretical analysis based on quasi-geostrophic theory sheds light on these findings and furthermore validates the numerical simulations. The simulated baroclinic instability waves on both the f- and β-plane matched the predicted wavelength, shape and linear growth rate obtained from the QG theory very well. Our results also suggest that the dynamics within a continuously stratified baroclinic instability differ from the results of a two-layer model of baroclinic instability. In the two-layer theory the addition of β tends to stabilize the flow, especially the very long waves, and reduces the corresponding instability. Our results with the most unstable wave modes between $\tilde{k}=10-12$ show that the β-plane is more unstable. However, our results also show that the growth rates of longer waves with $\tilde{k}<10$ are smaller in the β-plane simulation which is in general agreement with the two-layer QG theory.

Acknowledgement

Support for this research was provided through the U.S. Department of Energy (DoE) Office of Science under the grants DE-SC0006684 and DE-SC0003990.

References

Bretherton F. 1966. Baroclinic instability and the short wavelength cut-off in terms of potential vorticity. *Quart. J. Royal Meteor. Soc.* **92**(393): 335–345.

Charney JG. 1947. The dynamics of long waves in a baroclinic westerly current. *J. Meteor.* **4**(5): 136–162.

Davies DH, Schär C, Wernli H. 1991. The palette of fronts and cyclones within a baroclinic wave development. *J. Atmos. Sci.* **48**(14): 1666–1689.

Davis CA. 2010. Simulations of subtropical cyclones in a baroclinic channel model. *J. Atmos. Sci.* **67**(9): 2871–2892.

Eady E. 1949. Long waves and cyclone waves. *Tellus* **1**(3): 33–52.

Galewsky J, Polvani LM, Scott RK. 2004. An initial-value problem to test numerical models of the shallow water equations. *Tellus* **56A**: 429–440.

Heifetz E, Bishop C, Hoskins B, Methven J. 2004a. The counter-propagating Rossby-wave perspective on baroclinic instability. I: Mathematical basis. *Quart. J. Royal Meteor. Soc.* **130**(596): 211–231.

Heifetz E, Methven J, Hoskins B, Bishop C. 2004b. The counter-propagating Rossby-wave perspective on baroclinic instability. II: Application to the Charney model. *Quart. J. Royal Meteor. Soc.* **130**(596): 233–258.

Holton JR. 2004. *An introduction to dynamic meteorology*. Academic Press, Inc., Fourth edn. 535 pp.

Jablonowski C, Williamson DL. 2006a. A baroclinic instabilitiy test case for atmospheric model dynamical cores. *Quart. J. Roy. Meteor. Soc.* **132**(621C): 2943–2975.

Jablonowski C, Williamson DL. 2006b. A baroclinic wave test case for dynamical cores of General Circulation Models: Model intercomparisons. NCAR Tech. Note NCAR/TN-469+STR, National Center for Atmospheric Research, Boulder, Colorado. 89 pp., available from http://www.ucar.edu/library/collections/technotes/technotes.jsp.

Kasahara A. 1974. Various vertical coordinate systems used for numerical weather prediction. *Mon. Wea. Rev.* **102**: 509–522.

Laprise R. 1992. The Euler equations of motion with hydrostatic pressure as an independent variable. *Mon. Wea. Rev.* **120**: 197–207.

Majewski D, Liermann D, Prohl P, Ritter B, Buchhold M, Hanisch T, Paul G, Wergen W, Baumgardner J. 2002. The operational global icosahedral-hexagonal gridpoint model GME: Description and high-resolution tests. *Mon. Wea. Rev.* **130**: 319–338.

Methven J, Heifetz E, Hoskins B, Bishop C. 2005. The counter-propagating Rossby-wave perspective on baroclinic instability. Part III: Primitive-equation disturbances on the sphere. *Quart. J. Royal Meteor. Soc.* **131**(608): 1393–1424.

Mirzaei M, Zülicke C, Mohebalhojeh AR, Ahmadi-Givi F, Plougonven R. 2014. Structure, energy, and parameterization of inertia-gravity waves in dry and moist simulations of a baroclinic wave life cycle. *J. Atmos. Sci.* **71**: 2390–2414.

Phillips NA. 1957. A coordinate system having some special advantages for numerical forecasting. *J. Meteor.* **14**: 184–185.

Plougonven R, Snyder C. 2007. Inertia-gravity waves spontaneously generated by jets and fronts. Part I: Different baroclinic life cycles. *J. Atmos. Sci.* **64**(7): 2502–2520.

Reed KA, Jablonowski C. 2012. Idealized tropical cyclone simulations of intermediate complexity: a test case for AGCMs. *J. Adv. Model. Earth Syst.* **4**: M04 001, doi:10.1029/2011MS000099.

Rotunno R. 1994. An analysis of frontogenesis in numerical simulations of baroclinic waves. *J. Atmos. Sci.* **51**(23): 3373–3398.

Schär C, Wernli H. 1993. Structure and evolution of an isolated semi-geostrophic cyclone. *Quart. J. Roy. Meteor. Soc.* **119**: 57–90.

Simmons AJ, Burridge DM. 1981. An energy and angular-momentum conserving vertical finite-difference scheme and hybrid vertical coordinates. *Mon. Wea. Rev.* **109**: 758–766.

Simmons AJ, Hoskins BJ. 1978. The life cycles of some nonlinear baroclinic waves. *J. Atmos. Sci.* **35**(3): 414–432.

Skamarock WC, Klemp JB, Dudhia J, Gill DO, Barker DM, Duda MG, Huang XY, Wang W, Powers JG. 2008. A description of the Advanced Research WRF Version 3. NCAR Tech. Note NCAR/TN-475+STR, National Center for Atmospheric Research, Boulder, Colorado. 113 pp., available from http://www.ucar.edu/library/collections/technotes/technotes.jsp.

St-Cyr A, Jablonowski C, Dennis J, Thomas S, Tufo H. 2008. A comparison of two shallow water models with non-conforming adaptive grids. *Mon. Wea. Rev.* **136**: 1898–1922.

Staniforth A. 2012. Exact stationary axisymmetric solutions of the Euler equations on $\beta-\gamma$ planes. *Atmos. Sci. Lett.* **13**(2): 79–87.

Tan ZM, Zhang F, Rotunno R, Snyder C. 2004. Mesoscale predictability of moist baroclinic waves: Experiments with parameterized convection. *J. Atmos. Sci.* **61**(14): 1794–1804.

Terpstra A, Spengler T. 2015. An initialization method for idealized channel simulations. *Mon. Weather Rev.* doi:10.1175/MWR-D-14-00248.1. In

press.
Thorncroft CD, Hoskins BJ, McIntyre ME. 1993. Two paradigms of baroclinic-wave life-cycle behaviour. *Quart. J. Roy. Meteorol. Soc.* **119**(509): 17–55.
Ullrich PA, Jablonowski C. 2012. Operator-split Runge-Kutta-Rosenbrock (RKR) methods for non-hydrostatic atmospheric models. *Mon. Wea. Rev.* **140**: 1257–1284.
Ullrich PA, Melvin T, Jablonowski C, Staniforth A. 2014. A proposed baroclinic wave test case for deep-and shallow-atmosphere dynamical cores. *Quart. J. Roy. Meteorol. Soc.* **140**: 1590–1602.
Untch A, Hortal M. 2004. A finite-element scheme for the vertical discretization of the semi-Lagrangian version of the ECMWF forecast model. *Quart. J. Roy. Meteor. Soc.* **130**: 1505–1530.
Vallis GK. 2006. *Atmospheric and oceanic fluid dynamics*. Cambridge University Press: Cambridge, U.K.
Waite ML, Bartello P. 2006. The transition from geostrophic to stratified turbulence. *Journal of Fluid Mechanics* **568**: 89–108.
Waite ML, Snyder C. 2009. The mesoscale kinetic energy spectrum of a baroclinic life cycle. *J. Atmos. Sci.* **66**(4): 883–901.
Waite ML, Snyder C. 2013. Mesoscale energy spectra of moist baroclinic waves. *J. Atmos. Sci.* **70**(4): 1242–1256.
Wang S, Polvani LM. 2011. Double tropopause formation in idealized baroclinic life cycles: The key role of an initial tropopause inversion layer. *J. Geophys. Res. (Atmospheres)* **116**(D5): D05 108.
Weller H, Thuburn J, Cotter CJ. 2012. Computational modes and grid imprinting on five quasi-uniform spherical C grids. *Mon. Wea. Rev.* **140**(8): 2734–2755.
Zhang F. 2004. Generation of mesoscale gravity waves in upper-tropospheric jet-front systems. *J. Atmos. Sci.* **61**(4): 440–457.

A. Vertical η coordinate

The hybrid terrain-following η-coordinate (Simmons and Burridge 1981) comprises a pure pressure coordinate and a σ-component with $\sigma = p/p_s$. The pressure p at a vertical model level η is given by

$$p(x, y, \eta, t) = a(\eta)\, p_0 + b(\eta)\, p_s(x, y, t) \tag{42}$$

where the hybrid coefficients $a(\eta)$ and $b(\eta)$ are height-dependent and most often provided in tabular form (see for example Reed and Jablonowski (2012) for the 30-level configuration of NCAR's Community Atmosphere Model (CAM) version 5). We recommend choosing a setup with $p_0 = 10^5$ Pa and constant initial surface pressure $p_s = p_0$. This leads to the simplified expression

$$p(x, y, \eta, t = 0) = (a(\eta) + b(\eta))\, p_0 = \eta\, p_0\,. \tag{43}$$

In the discrete representation, the vertical direction is subdivided into N_{lev} model levels which are bounded by $N_{lev} + 1$ interface levels (denoted by the half indices $k + \frac{1}{2}$). The pressure at the interfaces is then given by

$$p_{k+\frac{1}{2}} = a_{k+\frac{1}{2}}\, p_0 + b_{k+\frac{1}{2}}\, p_s = \eta_{k+\frac{1}{2}}\, p_0 \tag{44}$$

with $\eta_{k+\frac{1}{2}} = a_{k+\frac{1}{2}} + b_{k+\frac{1}{2}}$ and $k = 0, 1, 2, \cdots N_{lev}$. The corresponding η_k values at the level centers (the full model levels) are determined via the average $\eta_k = \frac{1}{2}\,(\eta_{k+\frac{1}{2}} + \eta_{k-\frac{1}{2}})$. It follows $p_k = \eta_k\, p_0$.

Note that some GCMs (for example documented in Majewski *et al.* (2002) or Untch and Hortal (2004)) employ the alternative notation $p_{k+\frac{1}{2}} = a_{k+\frac{1}{2}} + b_{k+\frac{1}{2}}\, p_s$ where the coefficients $a_{k+\frac{1}{2}}$ are already multiplied with the reference surface pressure p_0 and given in Pa. If such coefficients are provided special care needs to be taken to recover the η positions. First, the model-specific value of p_0 needs to be determined as some models utilize the "standard atmosphere" value of 1.01325×10^5 Pa like Untch and Hortal (2004). Second, the pressure-based $a_{k+\frac{1}{2}}$ coefficients need to be divided by p_0 to yield the η coefficients at layer interfaces

$$\eta_{k+\frac{1}{2}} = \frac{a_{k+\frac{1}{2}}}{p_0} + b_{k+\frac{1}{2}}\,. \tag{45}$$

The latter can be linearly averaged as shown earlier to give the corresponding η value at a full model level.

B. Iterative Method for Channel Models with z-based Vertical Coordinates

The initial conditions for the baroclinc wave in the 3D Cartesian channel have been designed for pressure-based vertical coordinates with initially $\eta = \sigma = p/p_s$. For models with height-based vertical coordinates we suggest using Newton's method which is a root-finding technique. It yields the corresponding η-level for any desired z position to machine precision. Newton's method therefore avoids vertical interpolations of the initial data set and furthermore is easy to implement. The algorithm has already been described for e.g. baroclinic wave initial conditions on the sphere by Jablonowski and Williamson (2006a) (see their Appendix) and is briefly summarized here for completeness. In particular, the iterative method is given by

$$\eta^{n+1} = \eta^n - \frac{F(x, y, \eta^n)}{\frac{\partial F}{\partial \eta}(x, y, \eta^n)} \tag{46}$$

where the superscript $n = 0, 1, 2, 3, \ldots$ denotes the iteration count.

For a selected z-level of the height-based vertical coordinate the functions F and $\partial F/\partial \eta$ are determined by

$$F(x, y, \eta^n) = -g\, z + \Phi(x, y, \eta^n) \tag{47}$$

$$\frac{\partial F}{\partial \eta}(x, y, \eta^n) = -\frac{R_d}{\eta^n}\, T(x, y, \eta^n) \tag{48}$$

where Φ and T are provided by Eqs. (7) and (10), respectively.

The starting value $\eta^0 = 10^{-7}$ is recommended for all Newton iterations following Eq. (46) which corresponds to a model top of about 100 km. The convergence is achieved if η^0 is greater than zero and physically lies above the uppermost model level. Typically, Newton's method converges within a maximum of 25 iterations, and most often the convergence is already achieved in under ten iterations. Then the absolute error $|\eta - \eta^n|$ is decreased to machine precision. The resulting η-level for the location (x, y, z) can then be used for the computation of the analytical initial conditions at the location (x, y, η).

If the model requires the initialization of the pressure p, density ρ or potential temperature Θ they can be computed as follows. First, determine $\eta(x, y, z)$ via the iterative technique. Second, determine p, ρ and Θ via

$$p(x, y, \eta) = \eta(x, y, z)\, p_0 \tag{49}$$

$$\rho(x, y, \eta) = \frac{p(x, y, \eta)}{R_d\, T(x, y, \eta)} \tag{50}$$

$$\Theta(x, y, \eta) = T(x, y, \eta)\Big(\frac{p_0}{p(x, y, \eta)}\Big)^{\frac{R_d}{c_p}} \tag{51}$$

with the specific heat at constant pressure $c_p = 1004.5$ J kg^{-1} K^{-1}.

Figure Suppl. 1 depicts the initial zonal wind and relative vorticity with respect to the height coordinate. In addition, Figs. Suppl. 2 and Suppl. 3 show the corresponding initial temperature, pressure, potential temperature, absolute vorticity, Brunt-Väisälä frequency and Ertel's potential vorticity for both the f- and β-plane. We provide these figures to accommodate non-hydrostatic models with z coordinates and allow a straightforward comparison of the initial data set.

C. Inclusion of moisture

The analytical initial conditions for a moist variant of the baroclinic wave are almost identical to the dry configuration. The differences are that the original T equation (10) is now the definition of the virtual temperature T_v, the originally dry

surface pressure $p_s = p_0$ and geopotential are interpreted as the surface pressure and geopotential of the moist air, the definition of the density needs to utilize the virtual temperature, and an analytical expression for the specific humidity q is added. The wind initialization of the moist baroclinic wave is identical to the dry case.

A suggested zonally-symmetric specific humidity field is

$$\langle q(\eta)\rangle = \frac{q_0}{2}\begin{cases} 1+\cos\left[\frac{\pi(1-\eta)}{1-\eta_w}\right] & \text{if } \eta \geq \eta_w, \\ 0 & \text{otherwise,} \end{cases} \tag{52}$$

$$q(x,y,\eta) = \langle q(\eta)\rangle \times \exp\left[-\left(\frac{y}{\Delta y_w}\right)^4\right] \tag{53}$$

with the meridional width parameter $\Delta y_w = 3200$ km, the η-based width parameter $\eta_w = 0.3$ and the maximum specific humidity amplitude $q_0 = 0.018$ kg kg^{-1}.

The density of the moist air is defined by the ideal gas law

$$\rho(x,y,\eta) = \frac{p(x,y,\eta)}{R_d\, T_v(x,y,\eta)} \tag{54}$$

and utilizes the pressure p of the moist air. The formulation of the virtual temperature and specific humidity leads to the analytically balanced representation of the temperature

$$T(x,y,\eta) = \frac{T_v(x,y,\eta)}{1+0.608\, q(x,y,\eta)} \tag{55}$$

This temperature is colder than the original dry temperature (10). However, note that in the moist case the virtual temperature and moist pressure determine the strength of the pressure gradient term in the momentum equations. Since these are identical to the temperature and pressure in the dry case, the forcing by the pressure gradient term is the same in both the dry and moist variant of the baroclinic wave. Once moisture is specified the model simulation can be run with a simple large-scale condensation parameterization as in Reed and Jablonowski (2012), or more complex physical parameterizations, to provide the precipitation and latent heating feedbacks.

D. Numerical discretization of Sturm-Liouville problem

We define a discrete mesh over the domain $[0, L_y] \times [0, z^*_{top}]$ via

$$y_j = \left(j - \frac{1}{2}\right)\Delta y, \quad \text{and} \quad z^*_k = \left(k+\frac{1}{2}\right)\Delta z^*, \tag{56}$$

where $j \in \{1,\ldots,N_y\}$ and $k \in \{1,\ldots,N_z\}$ are y and z^* indices within the mesh, $\Delta y = L_y/N_y$ and $\Delta z^* = z^*_{top}/N_z$, and N_y and N_z denote the number of elements in each coordinate direction (chosen to be 60 and 30 in practice). Consequently, we define Ψ at $(y,z) = (y_j, z_k)$ as $\Psi_{j,k}$. Within the interior of the domain, (37) is discretized using central derivatives,

$$\left(\frac{\partial^2\Psi}{\partial y^2}\right)_{j,k} \approx \frac{\Psi_{j+1,k} - 2\Psi_{j,k} + \Psi_{j-1,k}}{\Delta y}. \tag{57}$$

The vertical derivative term is expanded as

$$\frac{1}{\rho_0}\frac{\partial}{\partial z^*}\left(\frac{f_0^2\rho_0}{N^2}\frac{\partial\Psi}{\partial z^*}\right) = \frac{f_0^2}{N^2\rho_0}\frac{\partial\rho_0}{\partial z^*}\frac{\partial\Psi}{\partial z^*} + \frac{f_0^2}{N^2}\frac{\partial^2\Psi}{\partial(z^*)^2}, \tag{58}$$

and each derivative term discretized as

$$\left(\frac{\partial^2\Psi}{\partial(z^*)^2}\right)_{j,k} \approx \frac{\Psi_{j,k+1} - 2\Psi_{j,k} + \Psi_{j,k-1}}{(\Delta z^*)^2}, \tag{59}$$

$$\left(\frac{\partial\Psi}{\partial z^*}\right)_{j,k} \approx \frac{\Psi_{j,k+1} - \Psi_{j,k-1}}{2\Delta z^*}. \tag{60}$$

At lateral boundaries we enforce the no-flux condition $\Psi = 0$, and so the second derivative in y becomes

$$\left(\frac{\partial^2\Psi}{\partial y^2}\right)_{1,k} \approx \frac{-12\Psi_{1,k} + 4\Psi_{2,k}}{3\Delta y^2}, \tag{61}$$

$$\left(\frac{\partial^2\Psi}{\partial y^2}\right)_{N_y,k} \approx \frac{-12\Psi_{N_y,k} + 4\Psi_{N_y-1,k}}{3\Delta y^2}. \tag{62}$$

At vertical boundaries we must enforce (38). By writing the vertical derivative terms at the lower boundary as

$$\left(\frac{\partial\Psi}{\partial z^*}\right)_{j,1} \approx \frac{1}{2}\left(\frac{\partial\Psi}{\partial z^*}\right)_{j,1/2} + \frac{1}{2}\left(\frac{\partial\Psi}{\partial z^*}\right)_{j,3/2}, \tag{63}$$

$$\left(\frac{\partial^2\Psi}{\partial(z^*)^2}\right)_{j,1} \approx \frac{1}{\Delta z^*}\left[\left(\frac{\partial\Psi}{\partial z^*}\right)_{j,3/2} - \left(\frac{\partial\Psi}{\partial z^*}\right)_{j,1/2}\right] \tag{64}$$

where half-indices denote element edges, we note that we can express the cell-centered vertical derivative in terms of a derivative across the upper edge and one at the boundary. Again using a centered approximation,

$$\left(\frac{\partial\Psi}{\partial z^*}\right)_{j,3/2} \approx \frac{\Psi_{j,2} - \Psi_{j,1}}{\Delta z^*}, \tag{65}$$

and at the lower boundary

$$\left(\frac{\partial\Psi}{\partial z^*}\right)_{j,1/2} \approx \frac{1}{(\overline{u}-c)}\left(\frac{\partial\overline{u}}{\partial z^*}\right)_{j,1}\Psi_{j,1}. \tag{66}$$

A similar approximation is applied at the upper boundary. After applying all approximations, we rearrange (37) to obtain a matrix system of the form

$$\mathsf{A}\boldsymbol{\Psi}_d = c\mathsf{B}\boldsymbol{\Psi}_d, \tag{67}$$

where $\boldsymbol{\Psi}_d$ is the vectorized form of $\Psi_{j,k}$. Since B is invertible, this system can be written as an eigenvalue problem of the form

$$\mathsf{F}\boldsymbol{\Psi}_d = c\boldsymbol{\Psi}_d, \tag{68}$$

where $\mathsf{F} = \mathsf{B}^{-1}\mathsf{A}$. This system can then be solved using standard numerical linear algebra techniques as e.g. provided in Matlab.